The Astrophysical Journal, 896:30 (27pp), 2020 June 10 https://doi.org/10.3847/1538-4357/ab9103

Determining the Composition of Relativistic Jets from Polarization Maps

Richard Anantua[1,2], Razieh Emami[1], Abraham Loeb[1,2], and Andrew Chael[3,4]
[1] Center for Astrophysics | Harvard & Smithsonian, 60 Garden Street, Cambridge, MA 02138, USA; ranantua@cfa.harvard.edu
[2] Black Hole Initiative at Harvard University, 20 Garden Street, Cambridge, MA 02138, USA
[3] Princeton Center for Theoretical Science, Jadwin Hall, Princeton University, Princeton, NJ 08544, USA
Received 2019 October 21; revised 2020 May 5; accepted 2020 May 5; published 2020 June 10

Abstract

We present a stationary, axisymmetric, self-similar, semianalytic model of magnetically dominated jet plasma based on force-free regions of a relativistic magnetohydrodynamic simulation. We use this model to illustrate how the composition of relativistic jet plasma can be determined, with special attention to the example of M87. In particular, we compute synthetic Stokes maps in e^-e^+p plasmas with various positron-to-proton ratios using synchrotron emission models to scale the partial pressure of electrons and positrons that emit at the observed frequency to the magnetic pressure, taking into account Faraday rotation and conversion. The lepton-dominated models produce bilaterally asymmetric radio intensity profiles with strong linear polarization and Stokes Q and U maps that are bilaterally asymmetric (but strongly correlated across the jet axis) and antisymmetric (and sometimes anticorrelated), respectively. The hadronic models produce more centrally brightened intensity and polarization maps. Circular polarization provides the cleanest observational tool for distinguishing the plasmas, as it increases outward from the jet core and central axis for highly ionic plasma, and is suppressed for pair-dominated plasma. We find a measurable degree of circular polarization V/I of $\mathcal{O}(10^{-2})$ for subequipartition hadronic jet plasmas averaged over milliarcsecond scales. Our stationary model predicts that the intensity-normalized autocorrelation functions of Q and U increase and decrease with frequency, respectively, for higher plasma betas in our parameter survey. On the other hand, the autocorrelation of V is sensitive to the frequency at lower betas. Multiband polarimetric observations could therefore be used as a novel probe of the composition of jet plasma.

Unified Astronomy Thesaurus concepts: Relativistic jets (1390); Magnetohydrodynamical simulations (1966); Magnetic fields (994); Supermassive black holes (1663); Quasars (1319); BL Lacertae objects (158)

1. Introduction

One of the most fundamental mysteries surrounding relativistic jets in active galactic nuclei (AGNs) is the relative proportion of positrons and protons in them (Begelman et al. 1984). Jet regions near the magnetic axis tend to be highly magnetized and are often modeled by invoking the Blandford–Znajek (BZ) mechanism (Blandford & Znajek 1977; McKinney et al. 2012), in which the BZ jet power scales as the squares of black hole spin and the horizon magnetic flux, and the electric potential drop across field lines is sufficient to produce e^-e^+ pairs that emit synchrotron radiation. Accretion disks at the base of these jets may be modeled as ion tori, providing varying degrees of pressure support for jets based on their thickness and density. An intermediate disk-jet region surrounding the BZ jet may be powered by hydrodynamic winds carrying ions from the disk in the Blandford–Payne (BP) mechanism (Blandford & Payne 1982). The ultimate composition of the low-density relativistic jet plasma depends sensitively on how efficiently ions are screened by the barrier of the rotating magnetic field lines around it.

Since over a century ago, when Heber Curtis observed a curious "straight ray" in the galaxy M87 (also known now to host the radio source 3C 274; Curtis 1918), observations of relativistic jets have increased in spatiotemporal resolution. Recent observations of AGN jets, such as the minute-scale variable 3C 279 in >100 MeV gamma-rays (Ackermann et al. 2016) and the M87 jet and counterjet (Walker et al. 2018) observed at 43 GHz with the Very Long Baseline Array (VLBA) and seen to be limb-brightened down to 7 Schwarszchild radii at 86 GHz by the Global millimeter-VLBI Array (GMVA; Kim et al. 2018) have challenged our understanding of particle acceleration of these most energetic multiwavelength astrophysical sources (Pierre Auger Collaboration 2017). Circular polarization measurements in 3C 279 attaining values as high as 1% indicate particle distribution functions so dominated by the low ($\gamma \ll 100$) end that Faraday rotation would preclude strong linear polarization if the jet were e^-p, thus suggesting positron dominance for that source (Wardle et al. 1998). Shocked ionic plasma can reasonably account for M87 boundary layers in centimeter intensity profiles, but the degree to which Doppler boosting and other jet particles affect the final images is uncertain. At smaller scales toward the jet base, other AGN components such as molecular clouds and the accretion disk may obscure the jet emission.

The advancement of millimeter very long baseline interferometry (VLBI) with the intercontinental network of baselines forming the Event Horizon Telescope (EHT) enabled observations of M87 at 230 GHz with a resolution down to the black hole horizon (Event Horizon Telescope Collaboration 2019). This allows direct comparison with general relativistic magnetohydrodynamic (GRMHD) simulations, such as high-accuracy relativistic magnetohydrodynamics (McKinney et al. 2003), which evolve plasma rest-mass density ρ, energy density u, velocity four-vector $v^\mu = \gamma(c, \boldsymbol{v})$, and magnetic four-vector[5] b^μ near black holes. However, there is still substantial uncertainty in the radiation physics that lights up these simulations, and how this physics changes at increasing radii from the black hole. To help free

[4] NASA Hubble Fellowship Program Einstein Fellow.

[5] Fluid frame magnetic four-vector b^μ is related to lab frame $B_\nu = \gamma(\boldsymbol{v}\cdot\boldsymbol{B}, \boldsymbol{B} - \boldsymbol{v}\times\boldsymbol{E})$ via $b^\mu = \frac{h^\mu_\nu B^\nu}{u^t}$, where the projection tensor $h^\mu_\nu = (v^\mu v_\nu + \delta^\mu_\nu)$.

ourselves from the constraints of the spatiotemporal dynamical range of the simulations, we step back and use a semianalytic model inspired by them. We endow this model with self-similarity, which enables us to model processes close to the black hole, such as the conversion of magnetic energy into pairs, as well as processes along the entire jet length, such as the buildup of current into magnetic towers (Fowler et al. 2019).

In the following, we compare jet plasmas across a range of possible compositions, from a pure electron–positron to predominately electron–proton plasma. The goal is to find decisive observational tests to distinguish these cases. To this end, we seek some observables that are sensitive to the charge-to-mass ratio of the particles. In particular, we expect the observed polarization to be dependent on plasma composition due to Faraday conversion and rotation effects (Marrone et al. 2007), and thus compute linear and circular polarization of an e^-e^+ plasma and compare autocorrelations of these maps with those of maps with an e^-p plasma.[6]

The contribution of the electrons is degenerate with that of the positrons, and their respective number densities appear additively in the radiative transfer functions relating to emission and linear polarization. The degeneracy is broken by the consideration of circular polarization, which cancels out for a symmetric e^+e^- plasma, but does not for an e^-p plasma. In what follows, we use protons and ions interchangeably because we do not expect observationally viable signatures to have a metallicity dependence due to the subdominant cosmic abundances of elements heavier than hydrogen. Jet composition has been addressed in previous analytic models, including that of Park & Blackman (2010), who find that ion number density and magnetic field strength have degenerate effects on the change in electric field phase angle through jet plasma; however, the semianalytic approach presented here self-consistently models emission as well as propagation.

The paper is organized as follows. In Section 2 we present the synchrotron formalism describing emission and absorption from a power distribution of electrons and positrons. In Section 3 we present a review of basic transfer equations for the synchrotron emission. In Section 4 we specify the parametric emission prescription for turning GRMHD variables into observable radiation from a given distribution of electrons, positrons, and protons. In Section 5 we present our stationary, self-similar, axisymmetric, semianalytic model, which we analyze through synthetic observations—Stokes maps, degree-of-polarization maps, and autocorrelations—in Section 6 over a parameter space spanning leptonic, pair, and evenly mixed plasmas over an observationally motivated range of β. We conclude in Section 7 with a summary of our main results and their implications.

[6] Note that the energy of particles contributing to polarized synchrotron emission is proportional to $m^{-3/2}$ (Rees 1968), where m refers to the mass of the radiating particle. Therefore we would expect that the total emission from the (e^-e^+) plasma is higher than the emission from the (e^-p) because protons are 1836 times heavier than electrons and do not significantly contribute to the synchrotron emission (unless their velocity distribution is greatly skewed toward c). There is also suppression of ionic power due to the $t_{\rm Syn,i}/t_{\rm Syn,e} \sim (m_p/m_e)^4$ slower synchrotron-cooling time for ions (Rees 1968). Thus, the direct contributions of ions to synchrotron radiation is neglected in our analysis.

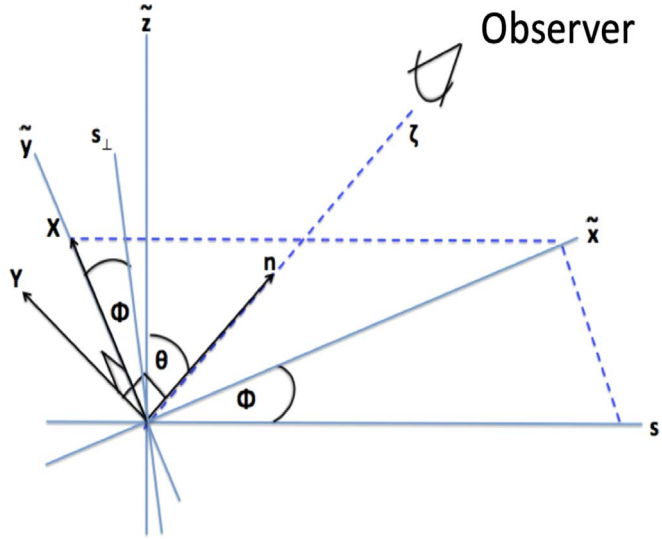

Figure 1. Polarization axes X and Y on the sky superposed onto galaxy Cartesian coordinates $\{\tilde{x}, \tilde{y}, \tilde{z}\}$ and galaxy cylindrical polar coordinates $\{s, \phi, \tilde{z}\}$. The displacement from the observer plane is parameterized by ζ and the inclination angle is θ. A jet propagating to length L along $\tilde{z}$ in the galaxy has a projected length $L\cos\theta$ along the observer Y-axis.

2. Synchrotron Formalism

We start by pedagogically constructing polarized emission $j'_{\nu\Omega}$ and absorption coefficients $\chi'_{\nu\Omega}$ from the particle distribution function $N'_{e\Omega'}$ per unit solid angle (where primes denote fluid comoving quantities). Polarized synchrotron radiation is characterized by emission and absorption coefficients that depend linearly on the partial pressure of electrons and positrons emitting near the observed frequency. The radiative transfer functions derived after specifying comoving electron+positron number density per unit solid angle (Anantua 2016), $N'_{e\Omega'}$, will enable us to implement emission models simply by specifying phenomenologically motivated partial pressures. Faraday conversion of circular to linear polarization also has a similar dependence, although Faraday rotation of linearly polarized light does not.

We start with coefficients of the radiative transfer equation in the emitting particle frame, then convert them into observer frame quantities by making use of the Lorentz invariance of $\nu\chi_\nu$ and j_ν/ν^2 and noting the Doppler factor,

$$\mathcal{D} = \frac{1}{\gamma\left(1 - \frac{v}{c}\cdot\hat{n}\right)} = \frac{\nu}{\nu'}, \tag{1}$$

where ν is the observed frequency, $\hat{n}$ is the direction along the line of sight (l.o.s.; see Figure 1), and primed quantities denote the particle frame. Then we solve the radiative transfer equation by l.o.s. integration of observer frame quantities. In the next subsection, we decompose emission and absorption onto the distant observer (XY-plane) using the basis set by the two independent polarization directions of an incoming photon. In what follows, we assume that emitting particles are isotropic in the emitting plasma rest frame.

2.1. Power-law Electrons and Positrons

First consider a power-law distribution of electron and positron energies,

$$N'_{e\Omega'}(\gamma') = K'_{e\Omega'}\gamma'^{-p},$$
$$K'_{e\Omega'} = \frac{1}{4\pi}(n'_{e^-} + n'_{e^+})(p-1). \quad (2)$$

Here γ' is the Lorentz factor of the emitting particles and n'_e is their combined number density. The partial pressure contribution from electrons and positions emitting at the observed frequency can be written as

$$\tilde{P}_e = \frac{4\pi}{3}\gamma'^2 N'_{e\Omega'}(\gamma')m_e c^2 = \frac{4\pi}{3}K'_{e\Omega'}m_e c^2\gamma'^{2-p}, \quad (3)$$

we note that the partial pressure at a particular observed frequency is dominated by synchrotron-radiating particles at a particular Lorentz factor rather than from the total distribution. We assume that the particles follow the fluid with $v^\mu_{e-} \approx v^\mu_{e+} \approx v^\mu$ (Ressler et al. 2015, 2017; Sadowski et al. 2016), although different particle species may have slight relative speeds (Bourouaine et al. 2018). We distinguish the thermal Lorentz factor, γ, from the bulk Lorentz factor, Γ.

2.2. Observing a Relativistic Emitter

When an observer is added to the formalism, it is natural to express the synchrotron radiation theory formulae in terms of quantities parallel to the l.o.s. and quantities along the polarization plane. In Figure 1 the polarization plane is on the sky and ζ is a coordinate along the l.o.s. in the direction $\hat{n}$. This introduces a viewing angle dependence through the boosted, projected ("effective") magnetic field,

$$B_e \equiv \mathcal{D}^{-1}|\boldsymbol{B}'_\perp| = \mathcal{D}^{-1}|\boldsymbol{B}' \times \hat{n}|. \quad (4)$$

Particle energy is linked to emitted photon frequency in cgs units by

$$\gamma'^2 \approx \frac{\nu'}{2\nu'_c}, \quad \nu'_c = \frac{3eB'_\perp}{4\pi m_e c}, \quad (5)$$

where $\gamma' = \gamma$ and $\mathcal{D} = \mathcal{D}'^{-1}$ due to their respective ν dependences. Although emission observed at any frequency comes from a range of energies, it is convenient to replace the observing frequency with twice the critical frequency in the analytical calculations below.

2.3. Emission and Absorption

The comoving frame emissivity and absorption coefficients can be derived from the power per unit frequency radiated by an electron gyrating around a magnetic field (Westfold 1959),

$$p'_{\nu'1,2}(x) = \frac{\sqrt{3}k_e e^3 B'_\perp}{m_e c^2} \times \left[\frac{x}{2}\left(\pm K_{2/3}(x) + \int_x^\infty K_{5/3}(x')dx'\right)\right],$$
$$x \equiv \frac{\nu'}{\nu'_c}, \quad (6)$$

where K_q is a modified Bessel function of imaginary argument, and 1 and 2 refer to two independent polarization directions and $\nu_c = \frac{3}{4\pi}\frac{eB_\perp}{m_e c}$. Then the comoving emissivity components for a power-law electron distribution are

$$\begin{aligned} j'_{\nu'\Omega'1,2} &= K'_{\Omega'}\left(\frac{\nu'_c}{\gamma'^2}\right)^{\frac{p-1}{2}} \int_0^\infty dx 2x^{\frac{p-3}{2}} p'_{\nu'1,2}(x) \\ &= \frac{\sqrt{3}k_e e^3 B'_\perp K'_\Omega}{m_e c^2}\left(\frac{3eB'_\perp}{4\pi\nu' m_e c}\right)^{\frac{p-1}{2}} \int_0^\infty dx x^{\frac{p-1}{2}} \\ &\quad \times \left(\pm K_{2/3}(x) + \int_x^\infty dx' K_{5/3}(x')\right) \\ &= \frac{1}{2\sqrt{3}}k_e e^2 \frac{eB'_\perp}{m_e c^2}K'_\Omega\left(\frac{3eB'_\perp}{2\pi\nu' m_e c}\right)^{\frac{p-1}{2}} \\ &\quad \times \frac{\Gamma\left(\frac{3p-1}{12}\right)\Gamma\left(\frac{3p+7}{12}\right)}{p+1}\left\{\frac{3p+5}{2}, 1\right\} \\ &= \frac{1}{4\sqrt{3}}\tilde{P}_e\left(\frac{r_e\nu'}{c}\right)\left(\frac{3eB'_\perp}{2\pi\nu' m_e c}\right)^{\frac{3}{2}} \\ &\quad \times \frac{\Gamma\left(\frac{3p-1}{12}\right)\Gamma\left(\frac{3p+7}{12}\right)}{p+1}\left\{\frac{3p+5}{2}, 1\right\}, \end{aligned} \quad (7)$$

and the comoving absorption is

$$\begin{aligned} \chi'_{\nu 1,2} &= -\frac{1}{m_e\nu'^2}\int d\gamma'\gamma'^2 \frac{d}{d\gamma'}\left(\frac{N'_{\gamma',\Omega'}}{\gamma'^2}\right)p'_{\nu'1,2}(\gamma) \\ &= \frac{\sqrt{3}(p+2)k_e e^3 B'_\perp K'_\Omega}{4m_e^2 c^2\nu'^2}\left(\frac{3eB'_\perp}{4\pi\nu' m_e c}\right)^{\frac{p}{2}} \\ &\quad \times \left(\pm K_{2/3}(x) + \int_x^\infty dx' K_{5/3}(x')\right) \\ &= \frac{1}{2\sqrt{3}}k_e e^2 \frac{eB'_\perp}{m_e c^2}K'_\Omega \frac{1}{\nu'^2}\left(\frac{3eB'_\perp}{2\pi\nu' m_e c}\right)^{\frac{p}{2}} \\ &\quad \times \Gamma\left(\frac{3p+2}{12}\right)\Gamma\left(\frac{3p+10}{12}\right)\left\{\frac{3p+8}{2}, 1\right\} \\ &= \frac{1}{4\sqrt{3}}\left(\frac{\tilde{P}_e}{m_e\nu'^2}\right)\left(\frac{r_e\nu'}{c}\right)\left(\frac{3eB'_\perp}{2\pi\nu' m_e c}\right)^2 \\ &\quad \times \Gamma\left(\frac{3p+2}{12}\right)\left(\frac{3p+10}{12}\right)\left\{\frac{3p+8}{2}, 1\right\}, \end{aligned} \quad (8)$$

where $\Gamma(\cdot)$ is the gamma function, $r_e = \frac{k_e e^2}{m_e c^2}$ is the classical electron radius, and $k_e = 1$ is the electrostatic constant.

The observer frame components of the emissivity and absorption coefficient associated with the independent polarization directions are found using the Lorentz transformation properties of emission, absorption, magnetic field, and frequency (Anantua 2016),

$$\begin{aligned} j_{\nu\Omega 1,2}(\nu, \hat{n}, \boldsymbol{B}) &= \mathcal{D}^4 P_S \frac{r_e \nu}{4\sqrt{3}c}\left(\frac{3eB_e}{2\pi\nu m_e c}\right)^{\frac{3}{2}} \\ &\quad \times \frac{\Gamma\left(\frac{3p-1}{12}\right)\Gamma\left(\frac{3p+7}{12}\right)}{p+1}\left\{\frac{3p+5}{2}, 1\right\}, \\ \chi_{\nu 1,2}(\nu, \hat{n}, \boldsymbol{B}) &= \mathcal{D}^4 P_S \frac{r_e}{4\nu\sqrt{3}c}\left(\frac{3eB_e}{2\pi\nu m_e c}\right)^{2} \\ &\quad \times \Gamma\left(\frac{3p+2}{12}\right)\Gamma\left(\frac{3p+10}{12}\right) \\ &\quad \left\{\frac{3p+8}{2}, 1\right\}, \end{aligned} \tag{9}$$

where there is a strong viewing angle dependence through $\mathcal{D} = \left(1 - \frac{|\boldsymbol{v}|}{c}\cos\theta\right)^{-1}$. The total emission and absorption coefficients per solid angle are then

$$\begin{aligned} j_{\nu\Omega} &\equiv j_{\nu\Omega 1} + j_{\nu\Omega 2} = \frac{3(p+1)}{3p+7}(j_{\nu\Omega 1} - j_{\nu\Omega 2}), \\ \chi_{\nu\Omega} &\equiv \frac{1}{2}(\chi_{\nu\Omega 1} + \chi_{\nu\Omega 2}) = \frac{3(p+2)}{3p+10}(\chi_{\nu\Omega 1} - \chi_{\nu\Omega 2}). \end{aligned} \tag{10}$$

We see that the emission is completely specified by P_S. Models based on this formalism (Anantua 2016; Blandford & Anantua 2017; Anantua et al. 2018) have used $P_S = \tilde{P}_e$; however, to compare plasmas with varying n_{e^+}/n_p, we may generalize to $P_S = f(\tilde{P}_e, \tilde{P}_i)$.

This methodology casts synchrotron emission and absorption functions in terms of the pressure $\tilde{P}_e$ due to electrons or positrons emitting at the observed frequency and the effective magnetic field $B_e = \mathcal{D}^{-1}|\boldsymbol{B} \times \hat{n}|$ for observer direction $\hat{n}$ (note that we perform slow light radiative transfer that does not approximate the speed of light as infinite). This formslism serves as the basis for one- or two-parameter models that show promising agreement with observations of AGN, e.g., M87 (Anantua et al. 2018).

3. Full Polarized Radiative Transfer

The full polarized radiative transfer equation in the fluid frame reads (Dexter 2016)

$$\frac{d}{ds}\begin{pmatrix} I' \\ Q' \\ U' \\ V' \end{pmatrix} = \begin{pmatrix} j'_I \\ j'_Q \\ j'_U \\ j'_V \end{pmatrix} - \begin{pmatrix} \chi'_I & \chi'_Q & \chi'_U & \chi'_V \\ \chi'_Q & \chi'_I & \rho'_V & \rho'_U \\ \chi'_U & -\rho'_V & \chi'_I & \rho'_Q \\ \chi'_V & -\rho'_U & -\rho'_Q & \chi'_I \end{pmatrix}\begin{pmatrix} I' \\ Q' \\ U' \\ V' \end{pmatrix}, \tag{11}$$

where (I', Q', U', V') refer to the Stokes parameters; j'_I, j'_Q, j'_U, j'_V represent the polarized emissivities; χ'_I, χ'_Q, χ'_U, χ'_V are the absorption coefficients; and ρ'_V and ρ'_Q, ρ'_U refer to one Faraday rotation and two Faraday conversion coefficients, respectively.

We wish to solve Equation (11) for different plasma compositions. We may simplify the analysis by aligning the magnetic field with the Stokes U' parameter to obtain $j'_U = \chi'_U = \rho'_U = 0$ (Dexter 2016). The most generic solution can then be achieved by performing a transformation that changes the polarization basis. In the following, we first compute the emissivity, absorption, Faraday rotation, and conversion functions in the $U' = 0$ basis. We then change the polarization basis and present the form of the transformation matrix to compute the remaining transfer parameters, i.e., j'_U, χ'_U and ρ'_U.

3.1. Polarized Emission, Absorption, and Faraday Coefficients in the $U' = 0$ Basis

Here we compute emissivity, absorption and Faraday coefficients in $U' = 0$ basis. We consider a plasma made of electrons, protons, and positrons. Due to the mass hierarchy, we ignore the direct contribution of protons to the radiative transfer equations and just keep them to guarantee the overall charge neutrality of the plasma.

We also generalize our power-law distribution function to electrons and positrons whose energies are truncated at some low and high Lorentz factors,

$$\begin{aligned} N'_{e\Omega'\gamma} &= \frac{1}{4\pi}N'_{e\gamma} \\ &= \begin{cases} \left(\frac{p-1}{4\pi}\right)(n'_{e^-} + n'_{e^+})(\gamma'^{1-p}_{\min} - \gamma'^{1-p}_{\max})^{-1}\gamma'^{-p} \equiv K'_{e\Omega\gamma}\gamma'^{-p} & , \gamma'_{\min} \leqslant \gamma' \leqslant \gamma'_{\max} \\ 0 & , \text{otherwise.} \end{cases} \end{aligned} \tag{12}$$

where $\gamma_{\min}$ and $\gamma_{\max}$ refer to the minimum and maximum particle Lorentz factors, respectively (see Appendix A).

Upon computing emissivity, absorption, and Faraday coefficients for an e^-e^+ plasma, we compare the results at each step with similar expressions in the literature. Because locally, the direction of motion of electrons and positrons around the magnetic field are in opposite senses, we adopt overall signs for their coefficients that are sensitive to the projection of the magnetic field vector along the wavevector. As shown below, this affects j'_V, α'_V, and ρ'_V.

We label quantities in the $U' = 0$ basis with a subindex 0.

3.1.1. Polarized Emissivity

In describing the polarized emissivity for an e^-e^+ plasma, we generalize the formalism described by Dexter (2016) to include positrons. The emissivity function for a power-law distribution of particles is given by appropriate linear combinations of (Dexter 2016)

$$j'^{IJ} = \int_0^\infty d\gamma' N'_\gamma \eta^{IJ}, \tag{13}$$

where η'^{IJ} refers to the 4×4 vacuum emissivity matrix given by Melrose (1971) and is defined in Equation (A1) of Dexter (2016).

We also directly compare our final results with Enßlin et al. (2019),

$$j' = \begin{pmatrix} j'_I \\ j'_Q \\ j'_U \\ j'_V \end{pmatrix} = j'_0 (n'_{e^-} + n'_{e^+}) B'^{(p+1)/2}_\perp \nu'^{\frac{1-p}{2}} \begin{pmatrix} 1 \\ q' \\ u' \\ v' \end{pmatrix}, \tag{14}$$

where we have

$$j'_{0I} = \frac{e^2}{c}\left(\frac{e}{2\pi m_e c}\right)^{\frac{p+1}{2}} (n'_{e^-} + n'_{e^+}) B'^{(p+1)/2}_\perp \nu'^{\frac{1-p}{2}} \times \left(\frac{3^{\frac{p}{2}}(p-1)}{2(p+1)}\right) \times \frac{\Gamma\left(\frac{3p-1}{12}\right)\Gamma\left(\frac{3p+19}{12}\right)}{(\gamma'^{1-p}_{\min} - \gamma'^{1-p}_{\max})}, \tag{15}$$

$$j'_{0Q} = \frac{p+1}{p+7/3} j'_{0I}, \tag{16}$$

$$j'_{0V} = \frac{e^2}{c}\left(\frac{e}{2\pi m_e c}\right)^{\frac{p+2}{2}} (n'_{e^-} - n'_{e^+}) B'^{(p+1)/2}_\perp \nu'^{\frac{1-p}{2}} \left(\frac{B'_\parallel}{\sqrt{\nu' B'_\perp}}\right) \times \left(\frac{3^{\frac{p-1}{2}}(p-1)(p+2)}{2p}\right) \frac{\Gamma\left(\frac{3p+4}{12}\right)\Gamma\left(\frac{3p+8}{12}\right)}{(\gamma'^{1-p}_{\min} - \gamma'^{1-p}_{\max})}, \tag{17}$$

where ν' refers to the comoving frequency. Our generalized formalism in the presence of positrons is in agreement with Enßlin et al. (2019).

3.1.2. Faraday Rotation Coefficients

Next, we generalize the Faraday rotation coefficients for an e^-e^+ plasma,

$$\rho'_{0V} = \left(\frac{e^3}{\pi m_e^2 c^2}\right)(n'_{e^-} - n'_{e^+}) \frac{(p-1)(p+2)}{(p+1)} \times \frac{\gamma'^{-(p+1)}_{\min} \ln(\gamma'_{\min})}{(\gamma'^{1-p}_{\min} - \gamma'^{1-p}_{\max})} B'_\parallel \nu'^{-2}. \tag{18}$$

Our final expression is consistent with Equation (A9) of Ruszkowski & Begelman (2002), who adopt a negative sign for the contribution of the positrons to ρ'_{0V}.

3.1.3. Faraday Conversion Coefficients

Next, we generalize the Faraday conversion coefficients for an e^-e^+ plasma,

$$\rho'_{0Q} = -\frac{e^4}{(2\pi)^2 (m_e c)^3} (n'_{e^-} + n'_{e^+}) B'^2_\perp \nu'^{-3} \times \frac{(p-1)\gamma'^{2-p}_{\min}}{(\gamma'^{1-p}_{\min} - \gamma'^{1-p}_{\max})} \times \left[\left(1 - \left(\frac{eB'_\perp}{2\pi m_e c \nu'} \gamma'^2_{\min}\right)^{p/2-1}\right)\left(\frac{p}{2} - 1\right)^{-1}\right] \tag{19}$$

(see Appendix B). Our final expression for the Faraday conversion is consistent with Equation (A8) of Ruszkowski & Begelman (2002), which has a positive sign for the contribution of positrons in ρ'_{0Q}.

3.1.4. Absorption Coefficients

Finally, we generalize the absorption coefficients for an e^-e^+ plasma,

$$\chi'_{0I} = \frac{e^2}{16 m_e c}\left(\frac{e}{2\pi m_e c}\right)^{\frac{p+2}{2}} 3^{\frac{p-1}{2}} (n'_{e^-} + n'_{e^+}) B'^{(p+2)/2}_\perp \nu'^{-\frac{p}{2}-2} \times (p-1)(3p+10) \frac{\Gamma\left(\frac{3p+10}{12}\right)\Gamma\left(\frac{3p+2}{12}\right)}{(\gamma'^{1-p}_{\min} - \gamma'^{1-p}_{\max})}, \tag{20}$$

$$\chi'_{0Q} = \frac{p+2}{p+10/3} \chi'_{0I}, \tag{21}$$

$$\chi'_{0V} = \frac{e^2}{4m_e c}\left(\frac{e}{2\pi m_e c}\right)^{\frac{p+3}{2}}(n_{e^-} - n_{e^+})B_\perp'^{(p+1)/2}\nu'^{-\frac{p+5}{2}}B_\parallel' \times \left(\frac{3^{\frac{p}{2}}(p-1)(p+2)(p+3)}{(p+1)}\right)\frac{\Gamma\left(\frac{3p+7}{12}\right)\Gamma\left(\frac{3p+11}{12}\right)}{(\gamma_{\min}'^{1-p} - \gamma_{\max}'^{1-p})}. \tag{22}$$

Again, our final results are based on the natural generalization of the approaches presented in Dexter (2016) and Jones & Odell (1977).

3.2. Transforming to Observer I, Q, U, and V

Given the comoving radiative transfer functions presented above, we now turn to the problem of expressing them in a convenient form for distant observers viewing a relativistic jet at frequency ν.

3.2.1. Transforming from Comoving to Observer Frame

The comoving quantities from Section 3.1 can be transformed into observer frame quantities by using the Lorentz invariance of $\nu'^{-2}j'_\nu$, $\nu'\chi'_\nu$ and $\nu'\rho'_\nu$ and the following dependencies on $\mathcal{D}$:

$$\frac{\nu}{\nu'} = \mathcal{D},$$
$$\frac{B_\perp}{B'_\perp} = \mathcal{D}^{-1},$$
$$B_\parallel = \Gamma\mathcal{D}^{-1}\left(B'_\parallel + \frac{\boldsymbol{B}\cdot\boldsymbol{v}}{\frac{1}{\Gamma} + \frac{1}{\Gamma+1}}\right). \tag{23}$$

3.2.2. The Orientation ψ of the Linear Polarization Ellipse

We start with the case of no circular polarization (Stokes $V = 0$) to focus on the relation between Q and U. The polarized radiative transfer equation for Stokes I, Q, and U reads

$$\frac{d}{ds}\begin{pmatrix} I \\ Q \\ U \end{pmatrix} = -\begin{pmatrix} \chi_I & \chi_Q & \chi_U \\ \chi_Q & \chi_I & 0 \\ \chi_U & 0 & \chi_I \end{pmatrix}\begin{pmatrix} I \\ Q \\ U \end{pmatrix} + \begin{pmatrix} j_1 + j_2 \\ (j_1 - j_2)\cos 2\psi \\ (j_1 - j_2)\sin 2\psi \end{pmatrix}, \tag{24}$$

where j_1 and j_2 are polarized emissivities associated with the two independent photon-polarization directions; the absorption coefficients are

$$\chi_I = \frac{\chi_1 + \chi_2}{2},$$
$$\chi_Q = \frac{(\chi_1 + \chi_2)\cos 2\psi}{2},$$
$$\chi_U = \frac{(\chi_1 + \chi_2)\sin 2\psi}{2}, \tag{25}$$

and the orientation angle in the observer (XY) plane is

$$\psi = \tan^{-1}(B_X^2 + B_Y^2 + E_X^2 + E_Y^2 - 2(E_X B_Y - E_Y B_X)). \tag{26}$$

The polarization plane is spanned by $\{\hat{\epsilon}_1, \hat{\epsilon}_2\}$. We note ψ is also the angle between the X-axis and the projection of the magnetic field onto the observer plane.

3.2.3. Changing the Polarization Basis from U = 0

We now recover the general radiative transfer case in which all terms may be nonzero. Choosing a polarization basis so that $j_U = 0 = \chi_0$ amounted to rotating the U subspace by 2ψ. We let

$$\boldsymbol{j}_0 = \begin{pmatrix} j_{0I} \\ j_{0Q} \\ 0 \\ j_{0V} \end{pmatrix}, \quad \boldsymbol{s}_0 = \begin{pmatrix} I_0 \\ Q_0 \\ U_0 \\ V_0 \end{pmatrix} = \begin{pmatrix} I_0 \\ Q_0 \\ 0 \\ V_0 \end{pmatrix}, \tag{27}$$

$$A_0 = \begin{pmatrix} \chi_I & \chi_Q & 0 & \chi_V \\ \chi_{0Q} & \chi_{0I} & \rho_{0V} & 0 \\ 0 & -\rho_{0V} & \chi_{0I} & \rho_{0Q} \\ \chi_{0V} & 0 & -\rho_{0Q} & \chi_{0I} \end{pmatrix}. \tag{28}$$

Then,

$$\frac{d\boldsymbol{s}_0}{d\zeta} = -A_0\boldsymbol{s}_0 + \boldsymbol{j}_0 \tag{29}$$

is the radiative transfer equation in the $U = 0$ basis.

Now, to transform this basis, let

$$P = \begin{pmatrix} 1 & 0 & 0 & 0 \\ 0 & \cos(2\psi) & \sin(2\psi) & 0 \\ 0 & -\sin(2\psi) & \cos(2\psi) & 0 \\ 0 & 0 & 0 & 1 \end{pmatrix}. \tag{30}$$

We identify

$$\frac{d(P^{-1}\boldsymbol{s}_0)}{d\zeta} = P^{-1}\boldsymbol{j}_0 - PA_0(P^{-1}\boldsymbol{s}_0) \tag{31}$$

with transformed radiative transfer equation

$$\frac{d\boldsymbol{s}}{d\zeta} = \boldsymbol{j} - A\boldsymbol{s}, \tag{32}$$

so we have

$$\boldsymbol{j} = \begin{pmatrix} j_I \\ j_Q \\ j_U \\ j_V \end{pmatrix} = P^{-1}\boldsymbol{j}_0 = \begin{pmatrix} j_{0I} \\ j_{0Q}\cos(2\psi) \\ j_{0Q}\sin(2\psi) \\ j_{0V} \end{pmatrix}, \tag{33}$$

$$A = \begin{pmatrix} \chi_I & \chi_Q & \chi_U & \chi_V \\ \chi_Q & \chi_I & \rho_V & \rho_U \\ \chi_U & -\rho_V & \chi_I & \rho_Q \\ \chi_V & -\rho_U & -\rho_Q & \chi_I \end{pmatrix} = PA_0P^{-1} \tag{34}$$

$$= \begin{pmatrix} \chi_{0I} & \chi_{0Q}\cos(2\psi) & -\chi_{0Q}\sin(2\psi) & \chi_{0V} \\ \chi_{0Q}\cos(2\psi) & \chi_{0I} & \rho_{0V} & \rho_{0Q}\sin(2\psi) \\ -\chi_{0Q}\sin(2\psi) & -\rho_{0V} & \chi_{0I} & \rho_{0Q}\cos(2\psi) \\ \chi_{0V} & -\rho_{0Q}\sin(2\psi) & -\rho_{0Q}\cos(2\psi) & \chi_{0I} \end{pmatrix}. \tag{35}$$

Thus, the matrix P manifestly rotates the QU subspace by 2ψ and serves to change the basis of the $U = 0$ absorption matrix to a generically rotated basis.

4. Emission Modeling

There is a plethora of plausible models representing jet emission phenomenology. Assuming jet emission is sourced by e^-e^+ plasma, Anantua et al. (2018) have employed a current density model with intensity dominated by a central jet "spine" (Hawley & Krolik 2006; Mościbrodzka et al. 2016) surrounded by return currents, and a shear model accentuating boundary layers. Moreover, a simple emission model we refer to as the constant electron–positron beta model (see the beta model of Anantua et al. 2018), where

$$\beta = \frac{P_g}{P_B} \tag{36}$$

converts a fraction of the electromagnetic energy density to gas (particle) energy density. We find this model to be naturally generalizeable to mixed leptonic/hadronic plasmas because an increase in ion number density is readily represented by a proportional reduction in the emitting electron partial pressure. We base our investigation of the effects of the plasma composition on jet Stokes maps on this class of models.

4.1. Constant β_e Model

We start with the constant electron–positron beta (β_e) model, where we equate the partial pressure $\tilde{P}_e$ due to a relativistic electrons-positrons gas to a constant fraction of the local magnetic pressure $P_B = \frac{B^2}{2}$,

$$\tilde{P}_e = \beta_{e0}P_B. \tag{37}$$

This model is a linear scaling of e^-e^+ gas pressure to local magnetic pressure with proportionality constant β_{e0}, although other scalings such as power laws have been devised, e.g., the magnetic bias model (Anantua et al. 2018).

4.1.1. Selection of the Parameter β_{e0}

Our simple emission model derives particle pressure from magnetic pressure throughout a jet segment at a constant "rate" β_{e0}. The partial pressure from synchrotron-emitting relativistic electrons and positrons can be estimated as

$$\tilde{P}_e \approx \frac{1}{3}\frac{\nu L_\nu t_{\rm cool}}{V_{\rm emit}}, \tag{38}$$

where $t_{\rm cool}$ is the synchrotron-cooling time and $V_{\rm emit}$ is the volume of the emitting region (modulo filling factor). Simulations show that the ratio of leptonic pressure to magnetic pressure $\beta_e = \frac{P_e}{P_B}$ tends to increase along the jet, while total β increases away from the axis towards the relativistically cold disk (McKinney & Blandford 2009; McKinney et al. 2012; Anantua 2016; Anantua et al. 2020). To estimate characteristic values of $\beta_{e0} \approx \frac{\tilde{P}_e}{P_B} \lesssim \beta_e$ for the M87 jet, we note that the observed jet geometry is given by Hada et al. (2016) to be paraboloidal ($s \propto z^{0.56}$) out to a deprojected distance $z \approx 200M$. The synchrotron luminosity can be deduced from the spectrum νF_ν in Prieto et al. (2016). For example, at 86 GHz, a deprojected radius of $11.41r_S$, parabolic width of $10.12r_S$, and flux density 0.16 Jy gives $\beta_{e0} \approx 9.2 \times 10^{-6}$ using a magnetic field supporting a jet magnetic flux of 10^{34} Mx $= 10^{26}$ Wb.

Equipartition of particle and magnetic energy densities, which may be brought about by magnetic reconnection, holds for $\beta_{e0} \sim 1$. We expect that the highly magnetized inner jet regions that we focus upon are subequipartition. As B drops with distance and the jet entrains particles (at a few $100M$ in our simulation, where $M \equiv GM_{\rm BH}/c^2$), the jet becomes mass loaded and particle dominated. To accommodate all of this physics, we construct an emission model for electrons, positrons, and protons to use in our semianalytic model.

4.2. Ionic Distribution Function

We now formally incorporate emission from a population of ions that have a power-law distribution into our polarized radiative transfer framework, although we expect their contribution to emission to be small. For simplicity, we think of them as protons:

$$N'_{i\gamma'} = K'_i\gamma'^{-p_i},\ \gamma'_{\rm min} \leqslant \gamma' \leqslant \gamma'_{\rm max}. \tag{39}$$

This might be generalized to other species, however, as long as we respect the overall charge neutrality of the plasma.

4.2.1. Ion Reduced Constant β_e Beta Model

Generalizing the e^-e^+ plasma constant electron beta model to plasmas for which $n = n_{e^-} + n_{e^+} + n_i = 2n_{e^-}$, we adopt

$$\tilde{P}_e = \frac{n - n_i}{n}\beta_{e0}P_B, \tag{40}$$

$$P_i = \frac{n_i}{n} P_g = \frac{n_i}{n}(\Gamma_{\rm E.o.S.} - 1) u_g, \tag{41}$$

$$\tilde{P}_i = \left(\frac{m_e}{m_p}\right)^{(4\ +\ 3)(p-1)/2} P_i \approx 0, \tag{42}$$

$$\tilde{P}_S = \tilde{P}_e + \tilde{P}_i \approx \tilde{P}_e. \tag{43}$$

where the equation of state parameter $\Gamma_{\rm E.o.S.}$ ranges from $4/3$ for relativistic particles to $5/3$ for nonrelativistic particles. The motivation for suppressing the contribution from ion pressure is, again, that protons emitting at the observed frequency are $(m_p/m_e)^{3/2}$ times as energetic as the corresponding electrons and that they cool $t_{\rm Syn,i}/t_{\rm Syn,e} \sim (m_p/m_e)^4$ slower. Thus we take the contribution of $\tilde{P}_i$ to our synthetic observations as 0. In our modeling, we also take $\gamma_{\rm min} = 10$ to be fiducial because $\gamma = 1$ gives the cyclotron radiation, and the synchrotron formalism above requires relativistic particles (Rybicki & Lightman 2004).

5. Self-similar Stationary Semianalytic Model

In order to implement our formalism to yield observables such as Stokes maps and electric vectors on the polarization plane, we employ a semianalytic model abstracted from the low-β, high-σ (i.e., the magnetic flux density and particle flux density, respectively) jet flow only $\lesssim 100M$ from the black hole in a GRMHD jet simulation with a dipole magnetic field and the thick, magnetically arrested disk initial conditions described in McKinney & Blandford (2009) and McKinney et al. (2012). Our model is stationary $\left(\frac{\partial}{\partial t} = 0\right)$ and axisymmetric $\left(\frac{\partial}{\partial \phi} = 0\right)$. This well approximates the azimuthally averaged simulation magnetohydrodynamic (MHD) variables in the jet region. For the parabolic jet in this model, the self-similarity variable is $\xi = \frac{s^2}{z}$, where s is the cylindrical radius and z is the altitude in our cylindrical coordinate system (see Figure 1).

We express—in cylindrical coordinates—the magnetic flux $\Phi = \Phi(\xi(s, z))$, current $I = I(\xi(s, z))$, and field-line angular velocity $\boldsymbol{\Omega}_B(\xi(s, z))$, and relate the jet variables to these as

$$\begin{pmatrix} B_s \\ B_\phi \\ B_z \end{pmatrix} = \begin{pmatrix} -\dfrac{1}{2\pi s}\dfrac{\partial \Phi}{\partial z} \\ \dfrac{I}{2\pi s} \\ \dfrac{1}{2\pi s}\dfrac{\partial \Phi}{\partial s} \end{pmatrix} = \begin{pmatrix} \dfrac{s\Phi'}{2\pi z^2} \\ \dfrac{I}{2\pi s} \\ \dfrac{\Phi'}{\pi z} \end{pmatrix}, \tag{44}$$

$$\boldsymbol{E} = \boldsymbol{B} \times (\hat{\Omega} \times \boldsymbol{r}), \tag{45}$$

$$\mu_0 \begin{pmatrix} j_s \\ j_\phi \\ j_z \end{pmatrix} = \nabla \times \boldsymbol{B} = \begin{pmatrix} -\dfrac{sI'}{2\pi z^2} \\ -\dfrac{s(2z\Phi' + (s^2 + 4z^2)\Phi'')}{2\pi z^4} \\ \dfrac{I'}{\pi z} \end{pmatrix}, \tag{46}$$

$$\frac{1}{\epsilon_0}\rho = \nabla \cdot \boldsymbol{E} = -\frac{1}{2\pi z^2}(\xi(4z + \xi)\Phi'\Omega_B' + \Omega_B(2(2z + \xi)\Phi' + \xi(4z + \xi)\Phi''), \tag{47}$$

using Ampère's law, Ohm's law for ideal MHD, Faraday's law, and Gauss' law, respectively. Assuming our jet plasma is force free,

$$\rho \boldsymbol{E} + \boldsymbol{j} \times \boldsymbol{B} = \boldsymbol{0}, \tag{48}$$

the current obeys

$$4\xi^2\omega_B^2\Phi'\Phi'' + 4\xi(\Omega_B^2 + \xi\Omega_B\Omega_B')\Phi'^2 = I'I, \tag{49}$$

with the solution

$$I = -2\Omega_B\xi\Phi'/Z_0. \tag{50}$$

To obtain numerical values in this semianalytic model, we fit $\Phi(\xi)$ and $\Omega_B(\xi)$ to azimuthally averaged $\boldsymbol{B}$, $\boldsymbol{v}$, ρ and u_g from the GRMHD simulation. We use the following fitting formulas:

$$\Phi(\xi) = \tanh(0.3\xi), \tag{51}$$

$$\Omega_B(\xi) = 0.15\exp(-0.3\xi^2). \tag{52}$$

The corresponding magnetic and velocity fields are

$$\begin{pmatrix} B_s \\ B_\phi \\ B_z \end{pmatrix} = \begin{pmatrix} \dfrac{\xi}{2\pi sz}\dfrac{\partial \Phi}{\partial \xi} \\ \dfrac{I}{2\pi s} \\ \dfrac{\xi}{\pi s^2}\dfrac{\partial \Phi}{\partial \xi} \end{pmatrix}, \quad \begin{pmatrix} v_s \\ v_\phi \\ v_z \end{pmatrix} = \begin{pmatrix} \dfrac{s}{2z}v_z \\ s\Omega_B(1 - v_z) \\ v_{z0}e^{-0.001s^8/z^4} \end{pmatrix}, \tag{53}$$

where $v_{z0}(z)$ is interpolated from the simulation using $v_{z0}(10) = 0.3c$, $v_{z0}(10^{1.7}) = 0.75c$, $v_{z0}(10^2) = 0.95c$, $v_{z0}(10^{3.5}) = 0.97c$ and $v_{z0}(10^4) = 0.99c$. For completeness, we also introduce the total gas-pressure fitting formula,

$$P_g(s) = 3.5 \times 10^{-7}(s/35)^3\exp(-(s/35)^4), \tag{54}$$

although this pressure contribution is neglected in the radiative transfer. The gas pressure rises from 0 at the jet axis to a maximum near the inflow/outflow boundary.

We are now in a position to construct numerical emission, absorption, and Faraday conversion and rotation functions from self-similar variables in this semianalytic model. Using the above

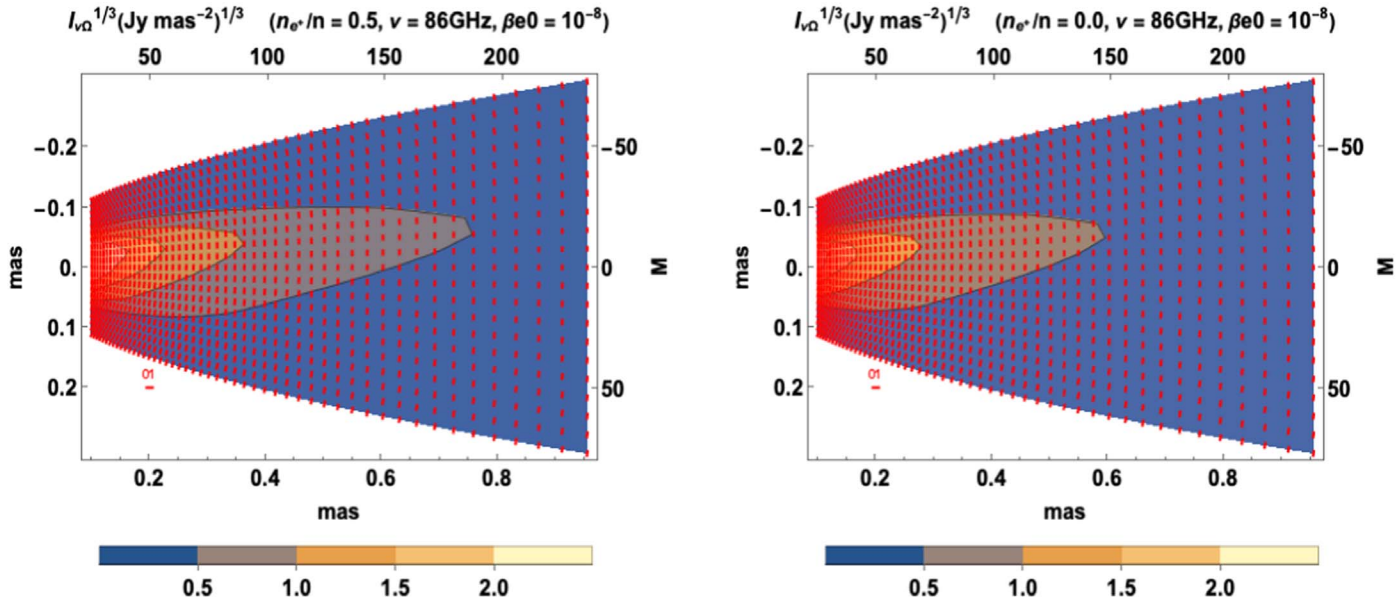

Figure 2. Images of intensity to the power of 1/3 at 86 GHz and $\beta_{e0} = 10^{-8}$ from ray-tracing the self-similar stationary semianalytic model for purely leptonic plasma $n_{e-} = n_{e+} = n/2$ (left) and a maximally hadronic plasma $n_{e-} = n_i = n/2$ (right). Polarization vectors (P_X, P_Y) are also shown (red), oriented at the EVPA.

fitting formulae, we can model jet physics on any scale in which the jet plasma is reasonably well represented by force-free GRMHD—even beyond the $\lesssim 10^5 M$ limit of modern jet simulations. Special relativistic effects are determined by the semianalytic velocity field, the observational frequency, and the viewing angle to the jet axis. We adopt a 20° viewing angle to emulate M87. Moreover, to convert our code-derived quantities into physical units for M87, we use a black-hole mass of $M_{\rm BH,M87} = 6.6 \times 10^9 M_\odot$ (Gebhardt et al. 2011) to obtain the length/time conversion $M \equiv r_{g,\rm M87} = \frac{GM_{\rm BH,M87}}{c^2} \approx 10^{13}$ m corresponding to the light-crossing time ≈9 hr, and a magnetic flux/field conversion $\Phi_{H,\rm M87} = \int_0^{s_{\max}(z)} 2\pi s B_z \approx 10^{26}$ Wb for the jet segments close to the black hole that we consider in the following.

6. Implementation

After presenting the generic formalism of how to compute the Stokes parameters in a mixed plasma, we now study different aspects of the Stokes maps for different observed frequencies as well as plasma parameters. Because the observations we focus on have been taken at two frequencies, 86 and 230 GHz, we show the behavior of the modeled system at these frequencies.

6.1. Intensity Maps

We first compare the case of $\beta_{e0} = 10^{-8}$ and $n_{e^-} = n/2 = n_{e^+}$ to the case with $n_{e-} = n/2 = n_i$, where n is the total particle number density. Figures 2 and 3 present the intensity map to power 1/3 at 86 GHz and 230 GHz, respectively. The plots are transformed by a one-third power $(\cdot)^{1/3}$ to increase contrast for the displayed quantities. The plots show a bilaterally asymmetric intensity map in the e^-e^+ plasma (left) and an inwardly shifted core of a map of lower intensity in the e^-p case (right); and a core-brightened polarization signature in both cases. For our synthetic observation, the horizontal axis on which the jet length is projected corresponds to the Y-axis of Figure 1, and the jet transverse direction is along the X-axis.

We have generated these and subsequent images in this work using the following effects.

6.1.1. Effects of the Plasma Composition at $\beta_{e0} = 10^{-8}$

Figure 2 shows that increasing the proton content (decreasing the positron content) diminishes the overall intensity at 86 GHz and shifts the core inward. The overall emission from the leptonic plasma is greater because there are more emitting particles than when half of the leptons are replaced by protons. The radiation electric vector determining the polarization direction can be written as

$$(P_X, P_Y) = \left(\sqrt{\frac{Q^2 + U^2 + Q\sqrt{Q^2 + U^2}}{2I^2}}, \times \sqrt{\frac{Q^2 + U^2 - Q\sqrt{Q^2 + U^2}}{2I^2}}\, \mathrm{sgn}(U) \right). \quad (55)$$

6.1.2. Effects of the Plasma Composition at $\nu = 230$ GHz

Figure 3 shows the same pattern of intensity decline with increasing ion content, now shifted farther inward for both compositions due to increased optical depth toward the core at 230 GHz. The core shift is accompanied by a slight upward shift of the contours within the finite observer plane segments of the maps, slightly enhancing the apparent bilateral asymmetry. A similar bilateral asymmetry has been observed by EHT for the quasar jet in 3C 279 at 230 GHz with 20 μas resolution (Kim et al. 2020). The bilateral asymmetry can be explained in the context of our models through the $\boldsymbol{B} \times \hat{n}$ dependence of B_e appearing in the partial pressure prescriptions for radiative

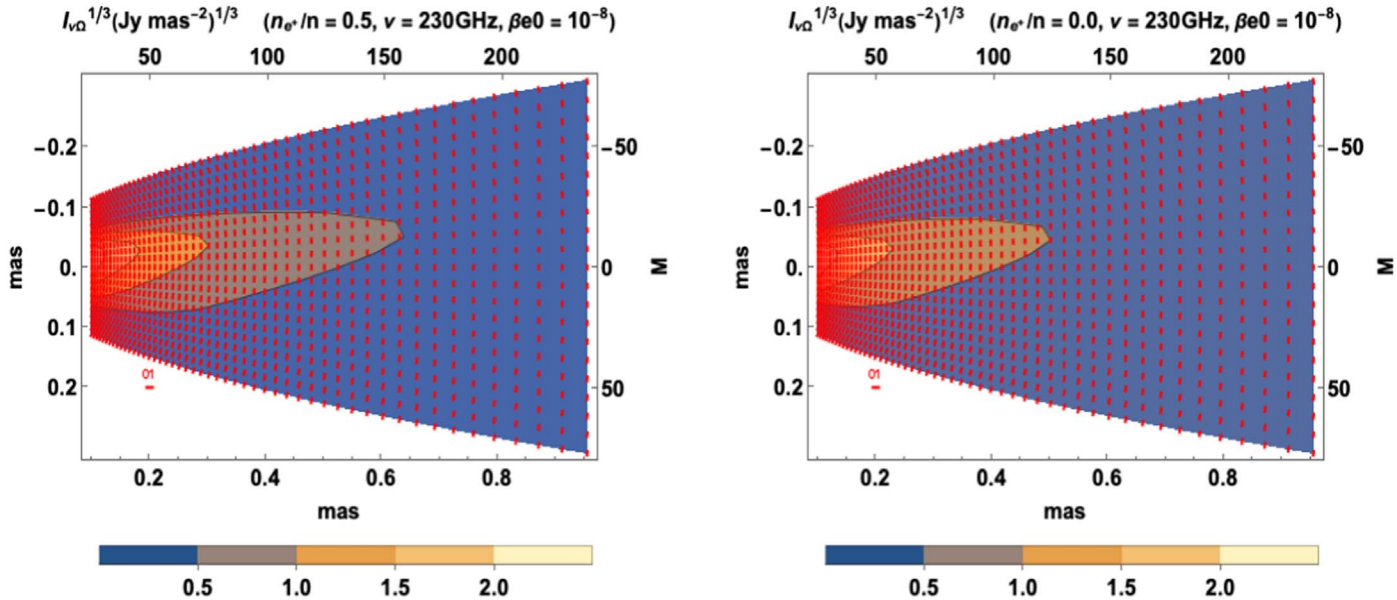

Figure 3. Images of intensity to the power of 1/3 at 230 GHz and $\beta_{e0} = 10^{-8}$ from ray-tracing the self-similar stationary semianalytic model for purely leptonic plasma $n_{e-} = n_{e+} = n/2$ (left) and a maximally hadronic plasma $n_{e-} = n_i = n/2$ (right). Polarization vectors (P_X, P_Y) are also shown (red), oriented at the EVPA.

transfer coefficients. As the helical jet field changes pitch angle, B_e varies across the jet axis (Blandford & Anantua 2017).

6.2. Stokes Map Symmetry Properties

Figures 4–12 compare Stokes maps across electron–positron beta constants ($\beta_{e0} = 10^{-10}$, 10^{-8} , and 10^{-6}), plasma compositions ($n_i/n = 0.0$, 0.25, and 0.5) and frequencies (86 and 230 GHz). We have shown all four Stokes parameters (overlaid by the same pattern of electric vectors) for each model parameter choice. The choice of representing polarization data using electric vector polarization angles (EVPA) overlaid on intensity maps versus displaying all Stokes maps is more than a cosmetic one–symmetry properties seen in the latter are often concealed in the former.

We begin our comparison with the lowest β_{e0} model with lowest ionic content presented in Figure 4, which has the most simply ordered contours: radiating outward from parabolic to elliptical for I, Q, and V, and dipolar for U. As the composition becomes increasingly leptonic from Figures 4–6, the dipolar pattern of U is mixed into V. Increasing the leptonic contribution increases the Stokes I parameter while suppressing the Stokes V parameter. As the frequency increases from 86 to 230 GHz, the maps tend to have higher overall amplitude emission, and V is less severely mixed.

By increasing the value of β_{e0} from 10^{-10} to 10^{-8}, we see that the higher β_{e0} maps in Figures 7–9 have higher overall amplitude emission and spatial distribution patterns degenerate with the highly ionic plasmas. We cleave some of this degeneracy by invoking autocorrelations in Section 6.2.10. When we increase to $\beta_{e0} = 10^{-6}$, mixing among the contour patterns in I, Q, and U increases and fine substructure appears in spotted regions near the jet core.

The most important trend, which can be seen in Figures 6, 9 and 12, is the disappearance of circular polarization, as quantified by the Stokes V parameter for purely symmetric e^+e^- plasmas ($n_{e^+}/n = 0.5$). Although the Stokes V parameter does not completely vanish even for the purely symmetric e^+e^- plasma because of the Faraday conversion, its value tends to be too low to be observable in this case. This distinct feature can therefore be used as a fingerprint of proton-deficient jets.

In summary, we see the following main patterns in the Stokes parameters for our model:

1. Bilateral asymmetry in intensity I, with maximum brightness toward the core
2. Bilateral asymmetry in one linear polarization, Q, whose polarization is maximized toward the core
3. Bilateral antisymmetry in the other linear polarization U (apparently rotated $\pi/4$ from Q)
4. Lower amplitude Stokes V, which vanishes for vanishing β_{e0} or n_i/n.

Another trend is that the symmetry of Q and antisymmetry of U is most apparent for the high-frequency, low-β_{e0}, low-n_{e^+}/n maps, in which the Q contours are ordered—from inward to outward—as slightly upward-shifted half-ellipses to parallelograms, and the U contours exhibit a simple dipolar pattern symmetric about $Y = 0$. At higher β_{e0}, particularly at lower frequencies, Q exhibits spotted features and V a dipolar pattern near the core with the negative part on the opposite side (here downward) as the highest positive intensity regions far away from the hole. At higher β_{e0} or n_{e^+}/n, Q becomes centrally brightened. As we lower the frequency and increase β_{e0} or n_{e^+}/n, a forward-oscillating pattern of polarity develops in U on the brightest side (here, upward), distorting the antisymmetry.

Observationally, we surmise that Q and U maps in the high-frequency, low-β_{e0} limits in which their contours are most ordered appear as 45% phase-shifted (see Anantua et al. 2018) versions of each other with opposite symmetric versus antisymmetric properties. When the order is perturbed by optical depth effects and stronger Doppler-beamed emission, the signature is less apparent.

6.2.1. Stokes Map Frequency Comparison for $n_{e^+}/n = 0.0$, $\beta_{e0} = 10^{-10}$

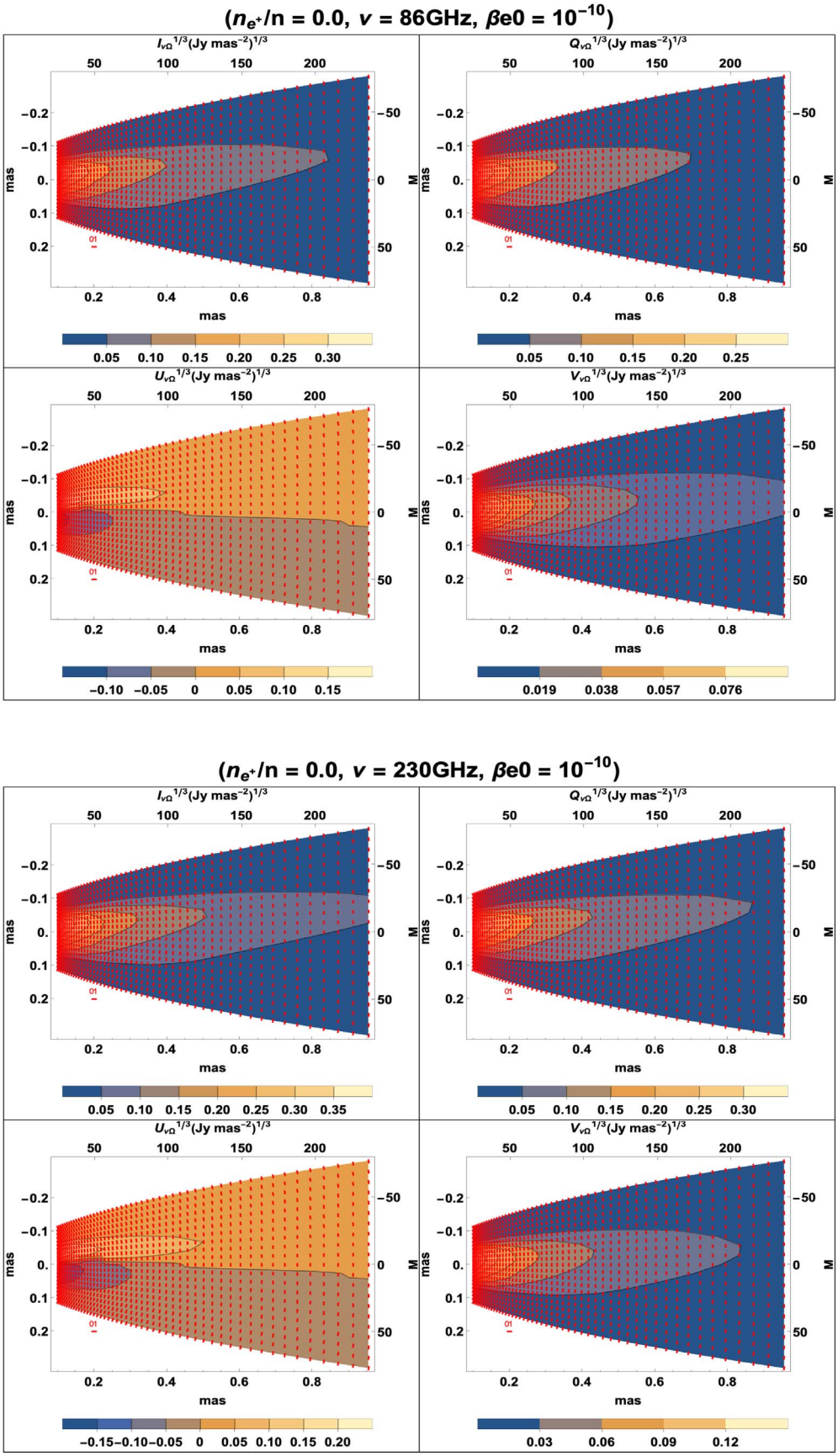

Figure 4. Stokes map (colors) overlaid with *E*-field vector orientations (red) with $\beta_{e0} = 10^{-10}$ at 43 GHz (upper) panel and at 230 GHz (lower) panel. We consider a maximally hadronic plasma with $n_{e+}/n = 0$ and for $\gamma_{\min} = 10$, $\gamma_{\max} = \infty$.

6.2.2. Stokes Map Frequency Comparison for $n_{e^+}/n = 0.25$, $\beta_{e0} = 10^{-10}$

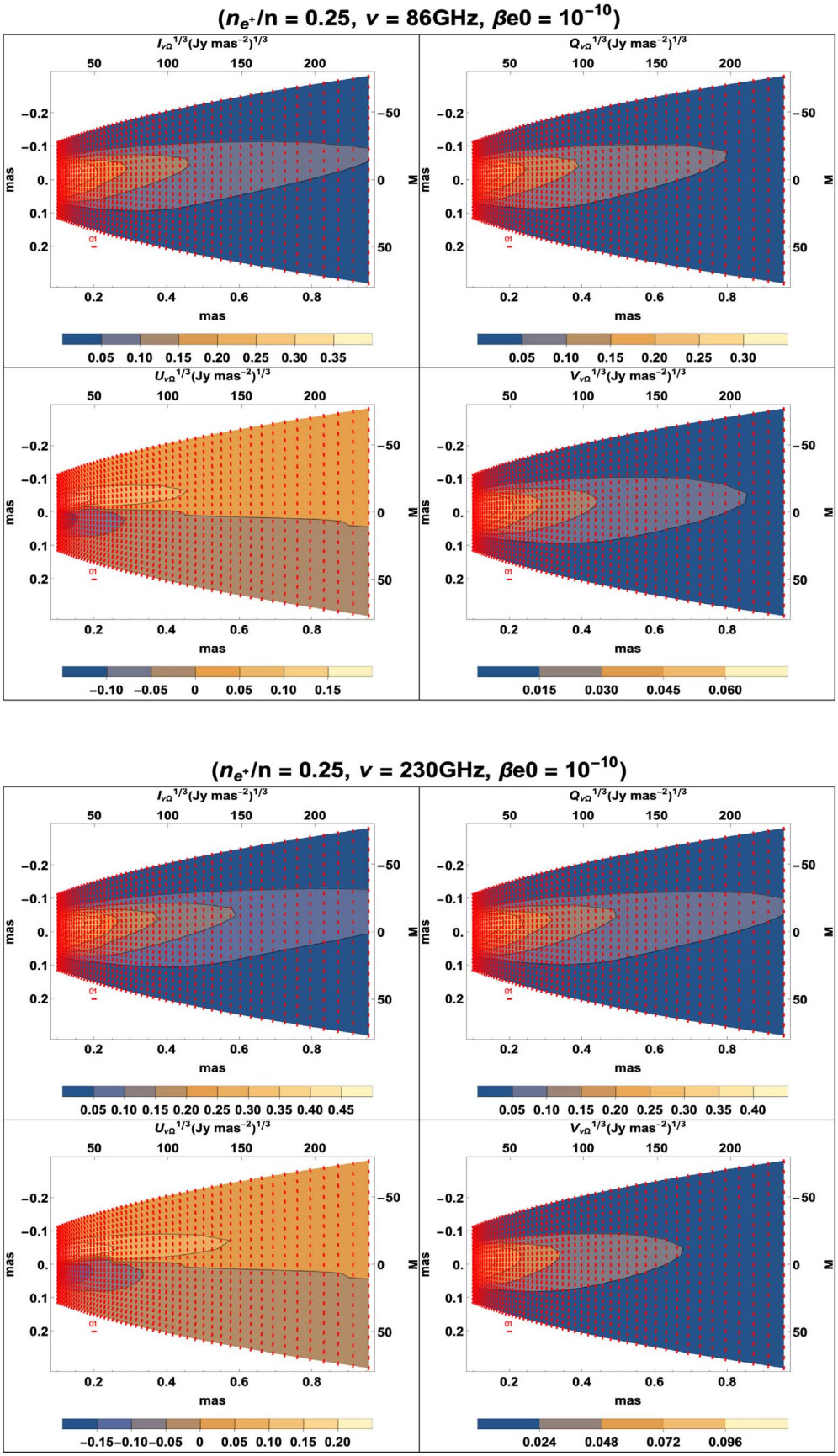

Figure 5. Stokes map (colors) overlaid with *E*-field vector orientations (red) with $\beta_{e0} = 10^{-10}$ at 43 GHz (upper) panel and at 230 GHz (lower) panel. We consider a midway hadronic plasma with $n_{e+}/n = 0.25$ and for $\gamma_{\min} = 10$, $\gamma_{\max} = \infty$.

6.2.3. Stokes Map Frequency Comparison for $n_{e^+}/n = 0.5$, $\beta_{e0} = 10^{-10}$

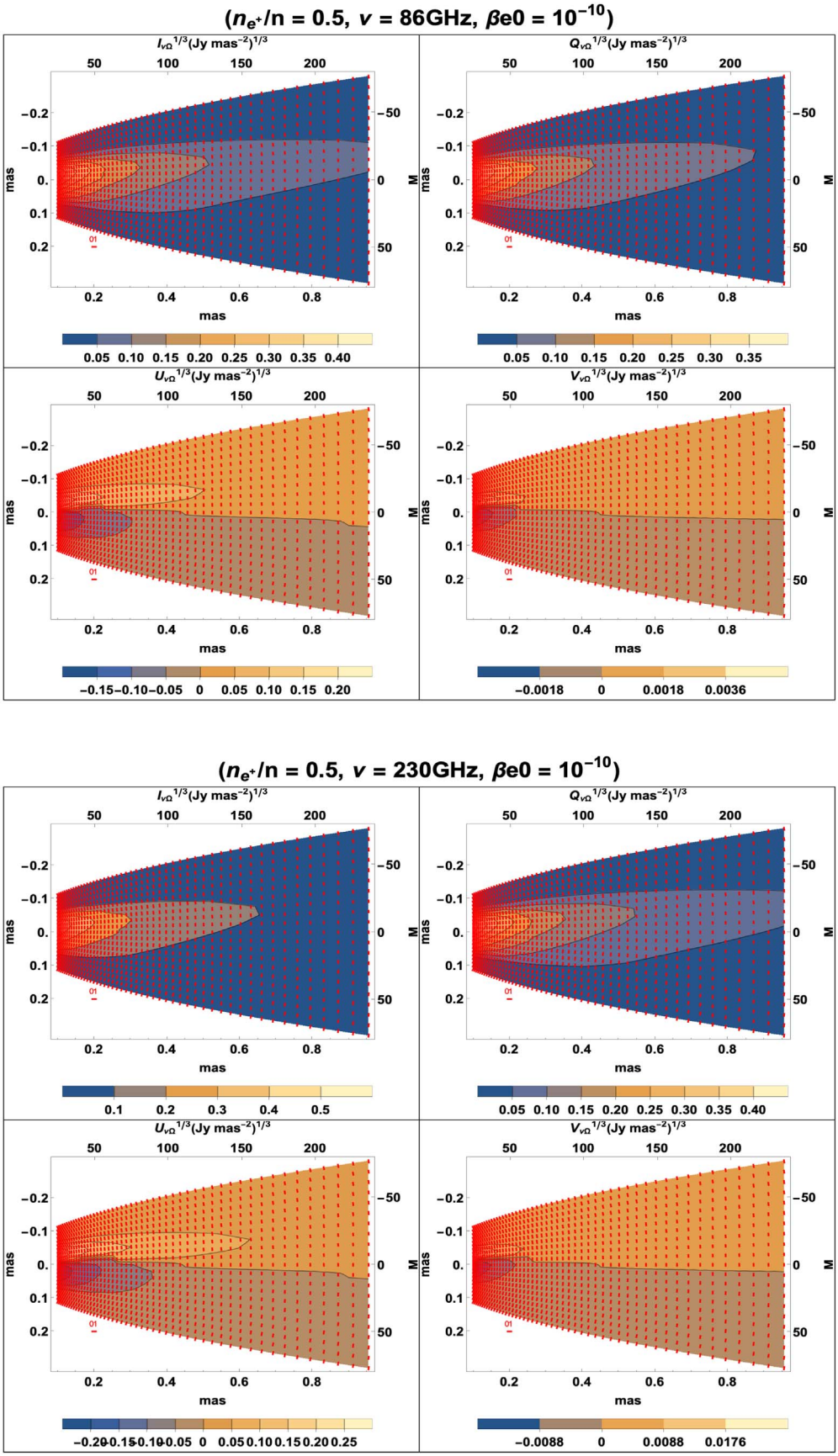

Figure 6. Stokes map (colors) overlaid with *E*-field vector orientations (red) with $\beta_{e0} = 10^{-10}$ at 86 GHz (upper) panel and at 230 GHz (lower) panel. We consider a maximally symmetric e^+e^- plasma with $n_{e+}/n = 0.5$ and for $\gamma_{\min} = 10$, $\gamma_{\max} = \infty$.

6.2.4. Stokes Map Frequency Comparison for $n_{e^+}/n = 0.0$, $\beta_{e0} = 10^{-8}$

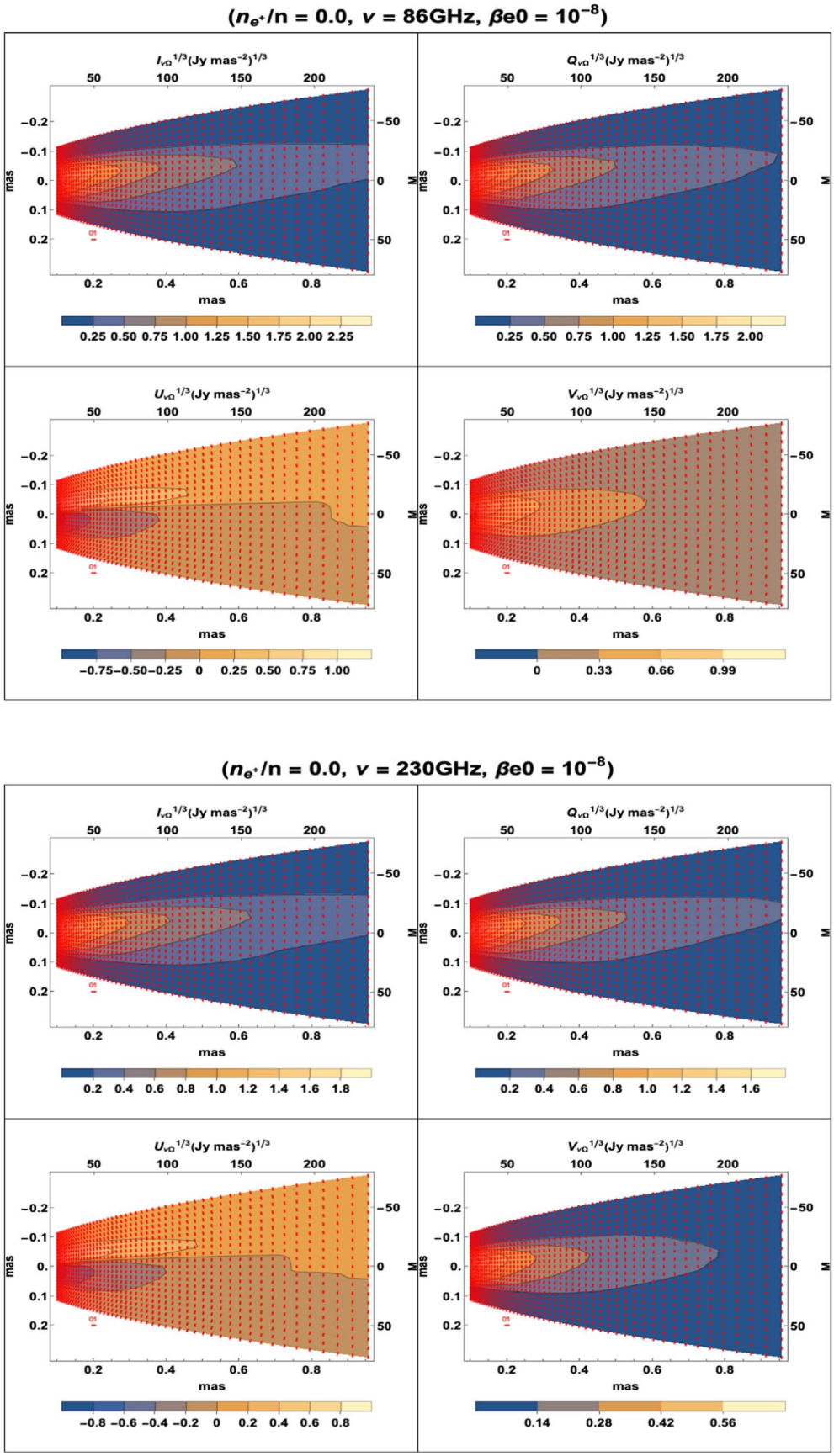

Figure 7. Stokes map (colors) overlaid with *E*-field vector orientations (red) with $\beta_{e0} = 10^{-8}$ at 86 GHz (upper) panel and at 230 GHz (lower) panel. We consider a maximally hadronic plasma with $n_{e+}/n = 0$ and for $\gamma_{\min} = 10$, $\gamma_{\max} = \infty$.

6.2.5. Stokes Map Frequency Comparison for $n_{e^+}/n = 0.25$, $\beta_{e0} = 10^{-8}$

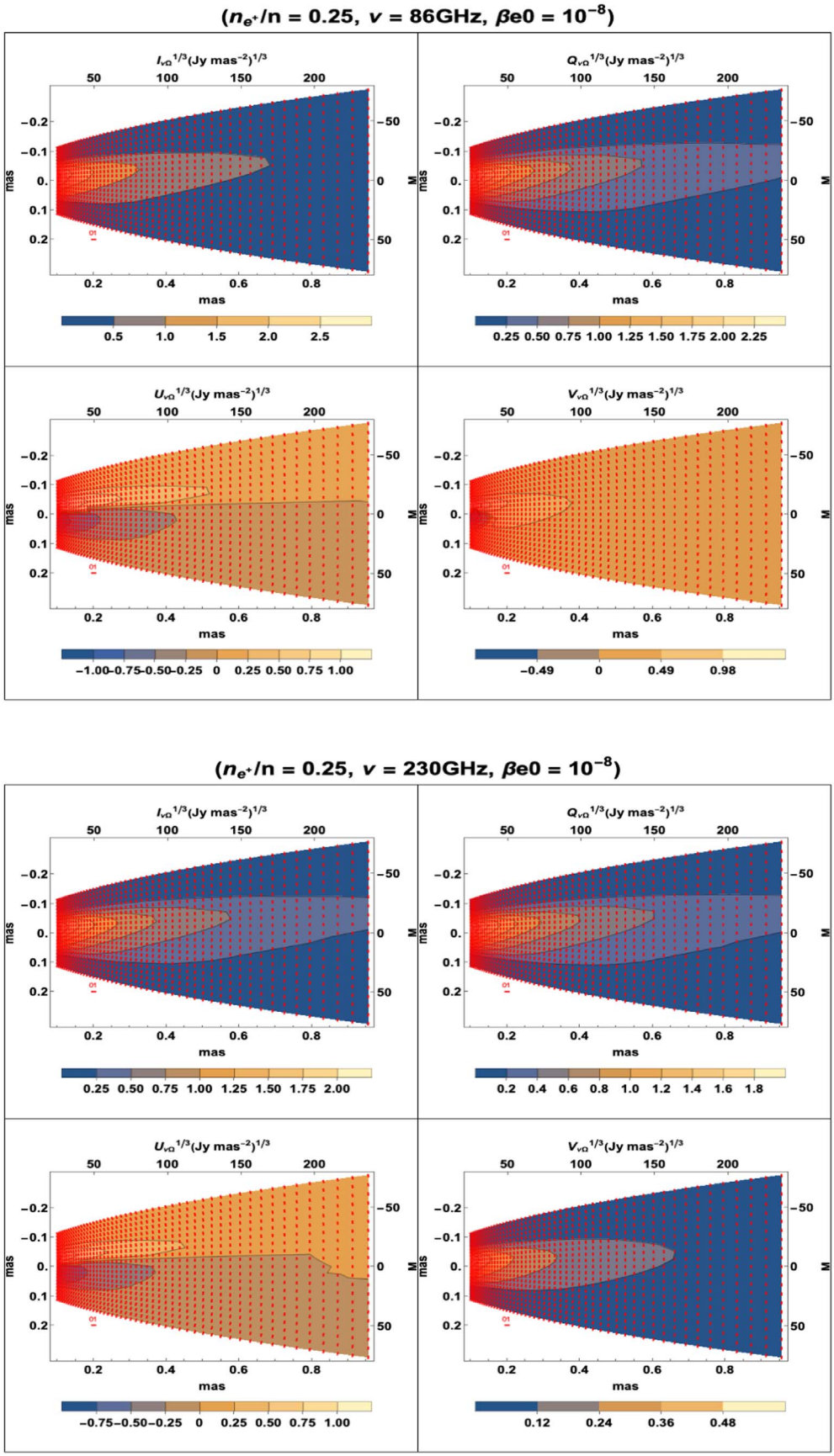

Figure 8. Stokes map (colors) overlaid with *E*-field vector orientations (red) with $\beta_{e0} = 10^{-8}$ at 86 GHz (upper) panel and at 230 GHz (lower) panel. We consider a midway hadronic plasma with $n_{e+}/n = 0.25$ and for $\gamma_{\min} = 10$, $\gamma_{\max} = \infty$.

6.2.6. Stokes Map Frequency Comparison for $n_{e^+}/n = 0.5$, $\beta_{e0} = 10^{-8}$

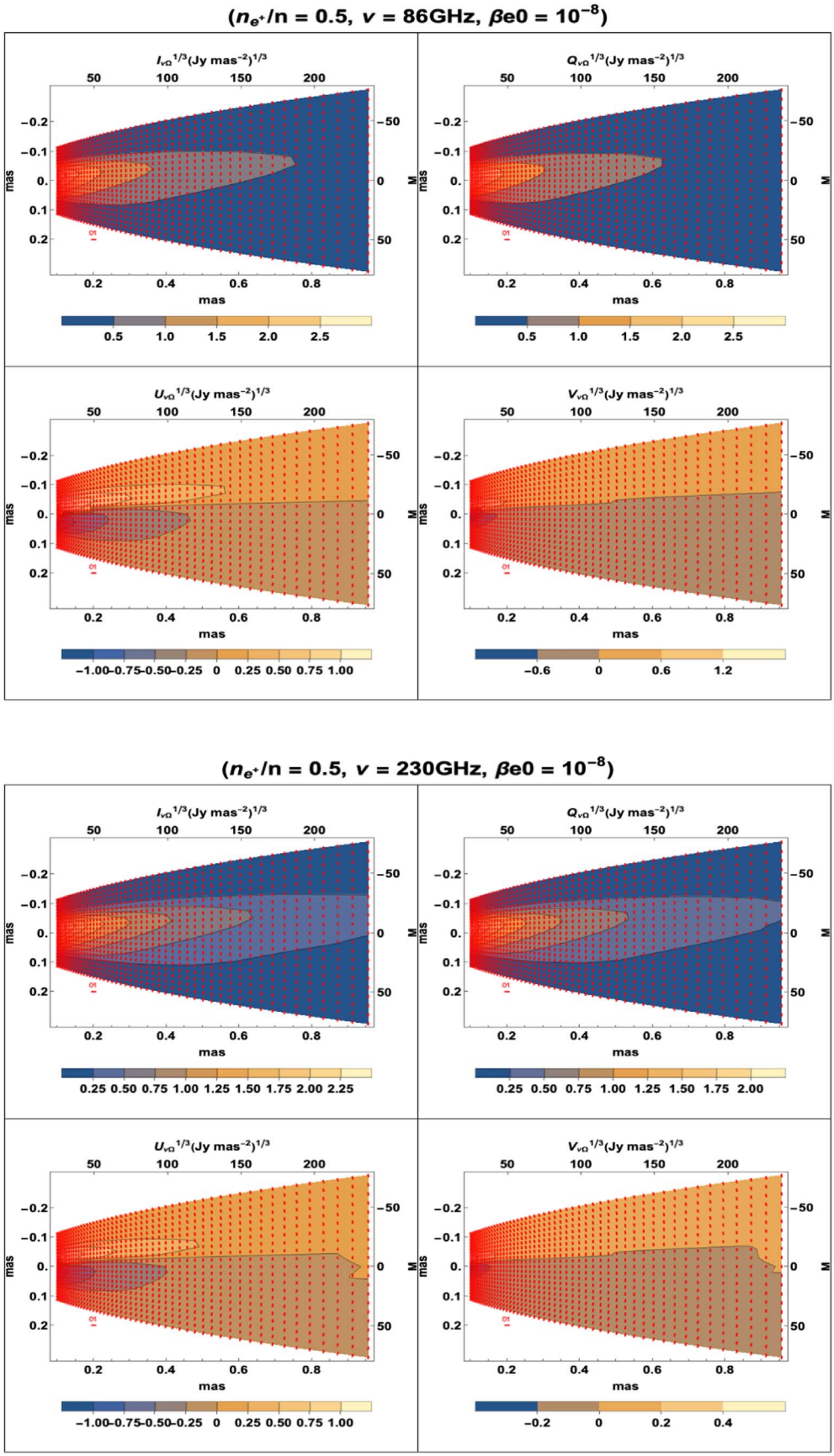

Figure 9. Stokes map (colors) overlaid with E-field vector orientations (red) with $\beta_{e0} = 10^{-8}$ at 86 GHz (upper) panel and at 230 GHz (lower) panel. We consider a maximally symmetric e^+e^- plasma with $n_{e+}/n = 0.5$ and for $\gamma_{\min} = 10$, $\gamma_{\max} = \infty$.

6.2.7. Stokes Map Frequency Comparison for $n_{e^+}/n = 0.0$, $\beta_{e0} = 10^{-6}$

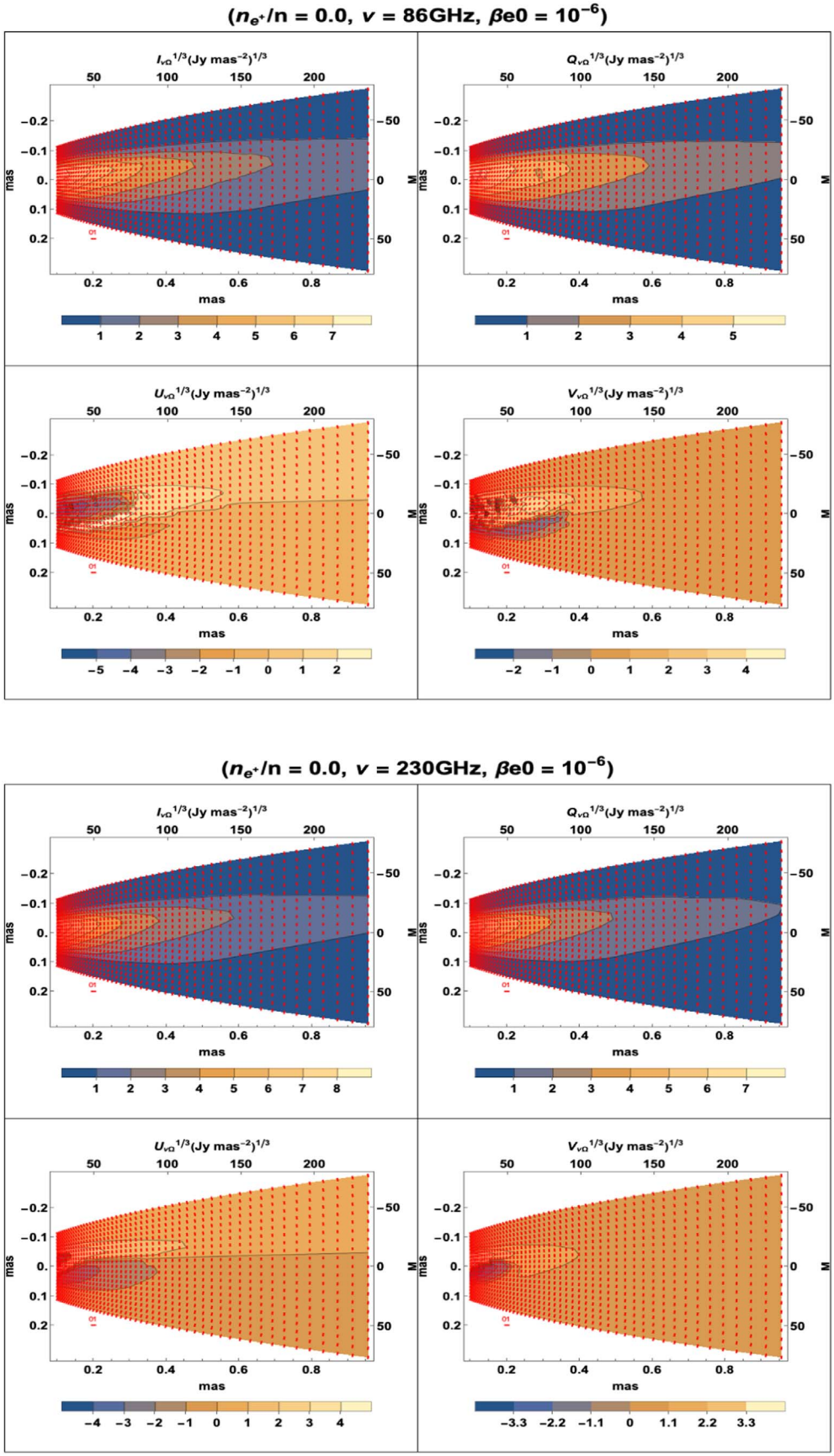

Figure 10. Stokes map (colors) overlaid with *E*-field vector orientations (red) with $\beta_{e0} = 10^{-6}$ at 86 GHz (upper) panel and at 230 GHz (lower) panel. We consider a maximally hadronic plasma with $n_{e+}/n = 0$ and for $\gamma_{\min} = 10$, $\gamma_{\max} = \infty$.

6.2.8. Stokes Map Frequency Comparison for $n_{e^+}/n = 0.25$, $\beta_{e0} = 10^{-6}$

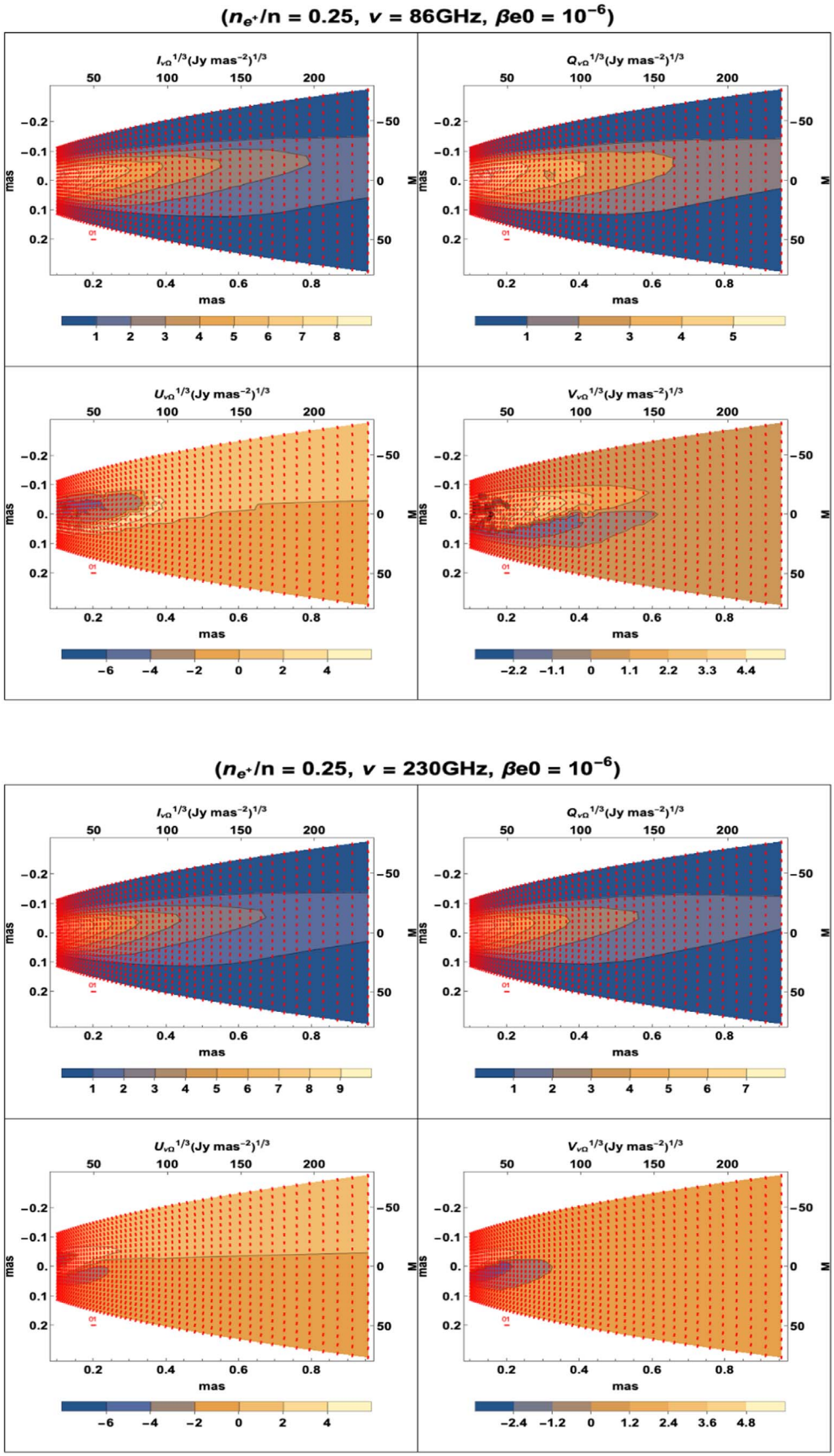

Figure 11. Stokes map (colors) overlaid with *E*-field vector orientations (red) with $\beta_{e0} = 10^{-6}$ at 86 GHz (upper) panel and at 230 GHz (lower) panel. We consider a maximally hadronic plasma with $n_{e+}/n = 0$ and for $\gamma_{\min} = 10$, $\gamma_{\max} = \infty$.

6.2.9. Stokes Map Frequency Comparison for $n_{e^+}/n = 0.5$, $\beta_{e0} = 10^{-6}$

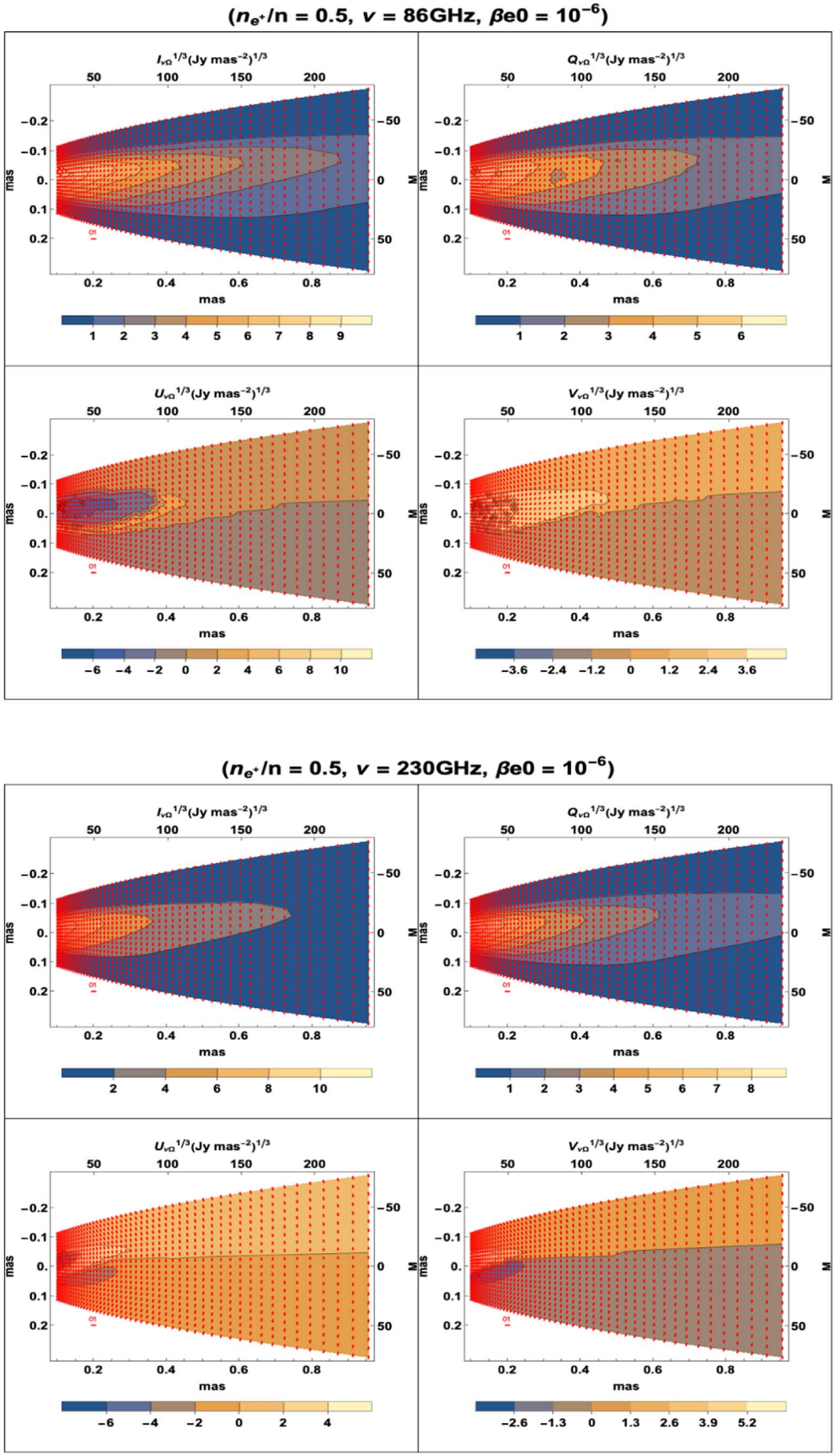

Figure 12. Stokes map (colors) overlaid with *E*-field vector orientations (red) with $\beta_{e0} = 10^{-6}$ at 86 GHz (upper) panel and at 230 GHz (lower) panel. We consider a maximally symmetric e^+e^- plasma with $n_{e+}/n = 0.5$ and for $\gamma_{\min} = 10$, $\gamma_{\max} = \infty$.

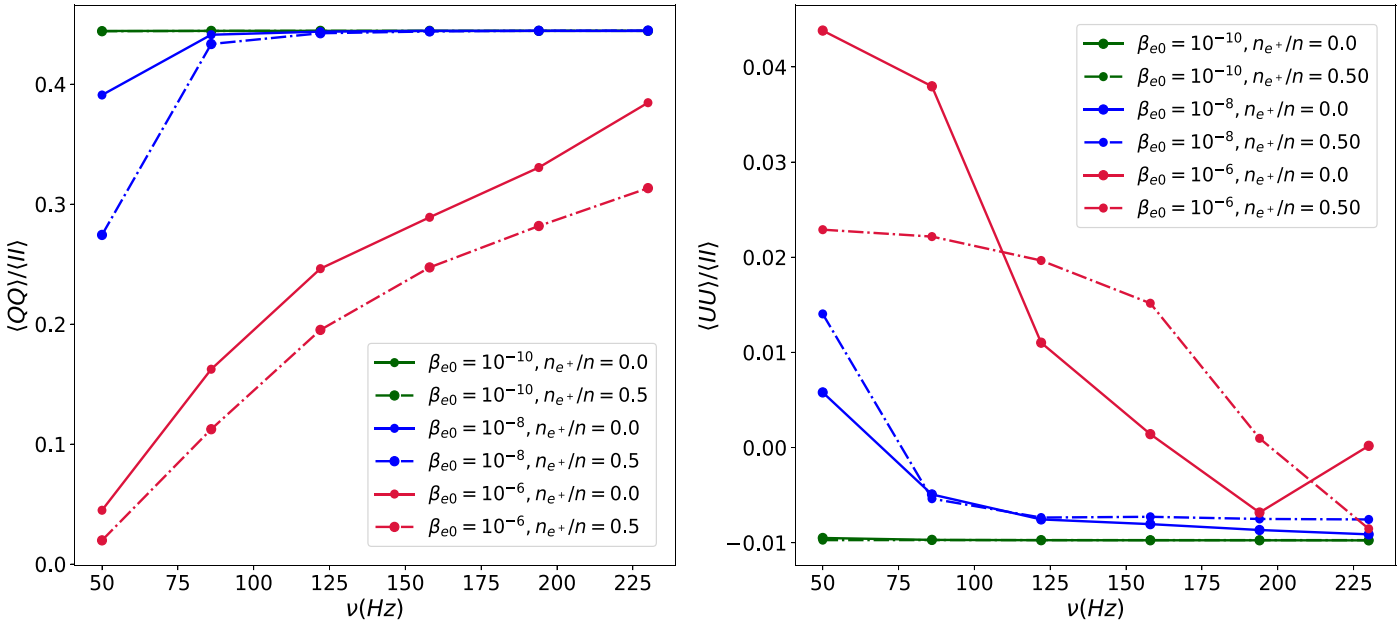

Figure 13. Autocorrelation ratios $\langle QQ\rangle/\langle II\rangle$ (left) and $\langle UU\rangle/\langle II\rangle$ (right) as functions of frequency for different values of $\beta_{e0} = 10^{-10}$, 10^{-8} and 10^{-6} and plasma compositions $n_{e^+}/n = 0.0$ and 0.5.

6.2.10. Autocorrelation Analysis

Next, we calculate the autocorrelation[7] functions of the Stokes parameters, where for a parabolic jet propagating in the Y direction, this is defined as

$$\langle ss\rangle = \int_{X_{\min}}^{X_{\max}} dX \int_0^{Y_{\max}} dY\, s(X, Y)s(X, -Y),$$
$$s \in \{I, Q, U, V\}. \tag{56}$$

Here the integrals are taken over the entire map for each Stokes parameter, as presented in Figures 4–12. We start with computing the autocorrelations of Q and U as functions of frequency. The autocorrelation functions are very useful parameters to exhibit the symmetry and antisymmetry patterns of the Stokes Q and U parameters. In the following, we normalize these autocorrelation functions to the function of the Stokes parameter I. Figure 13 presents $\langle QQ\rangle/\langle II\rangle$ and $\langle UU\rangle/\langle II\rangle$ for different values of β_{e0} as well as different plasma compositions, where again we adopt $\gamma_{\min} = 10$ and $\gamma_{\max} = \infty$.

The symmetric and antisymmetric patterns of the Stokes maps presented in Section 6.2 are replicated in the autocorrelation functions through a sign difference between the Q and U autocorrelations for most parameter values in Figure 13. This is more readily achieved for lower values of β_{e0} and for higher frequencies. Increasing the positron content n_{e^+}/n decreases the (positive) $\langle QQ\rangle/\langle II\rangle$ autocorrelations, but does not have a definite effect on the sign of the (positive or negative) $\langle UU\rangle/\langle II\rangle$ autocorrelations for our model parameters. The positive autocorrelations for Q in Figure 13 intuitively reflect the symmetry in its maps about $Y = 0$. At higher frequencies and for lower values of β_{e0}, U displays its anticipated antisymmetry (note that this is the orthogonal polarization to Q). However, at lower frequencies, the U map contours bow downward in a manner providing large positive contributions to the autocorrelation for low $|Y|$. This leads to a net positive autocorrelation for U in these cases.

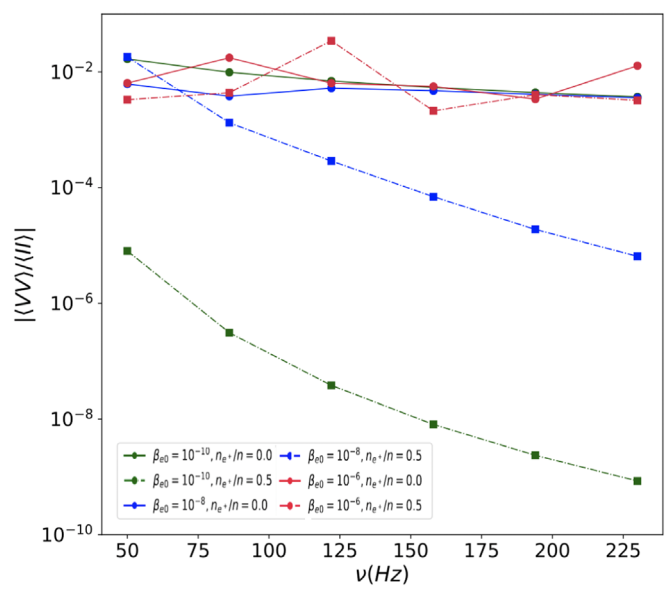

Figure 14. Autocorrelation ratio $|\langle VV\rangle/\langle II\rangle|$ (logarithmically scaled) as a function of frequency for different values of $\beta_{e0} = 10^{-10}$, 10^{-8} and 10^{-6} and plasma compositions $n_{e^+}/n = 0.0$ and 0.5.

Figure 13 gives us the following predictions:

1. Increasing the frequency increases (decreases) the value of $\langle QQ\rangle/\langle II\rangle$ ($\langle UU\rangle/\langle II\rangle$), respectively.
2. Higher values of β_{e0} enhance the autocorrelation of Stokes I faster than that of Q. Therefore the quantity $\langle QQ\rangle/\langle II\rangle$ decreases with increasing β_{e0}.

[7] Strictly speaking, the autocorrelation of a real valued function f, $\langle ff\rangle(\tau) \equiv \int_{-\infty}^{\infty} f(t)f(t-\tau)dt$, is the integral of the function times the function at a constant lag. Here, we extend the definition to the integral of a function times the function at a multiplicative scaling of the argument. Alternatively, we may use the definition of convolution ($(g * h)(\eta) \equiv \int_{-\infty}^{\infty} g(\hat{Y})h(\eta - \hat{Y})d\hat{Y}$) to express $\langle ss\rangle = \int_{-\infty}^{\infty} (s * s)(0)d\hat{X}$, where $\hat{X} = X$ if $|X| < X_{\max}$, 0 otherwise, and analogously for Y, as the integral of the convolution of s with itself centered at $Y = 0$.

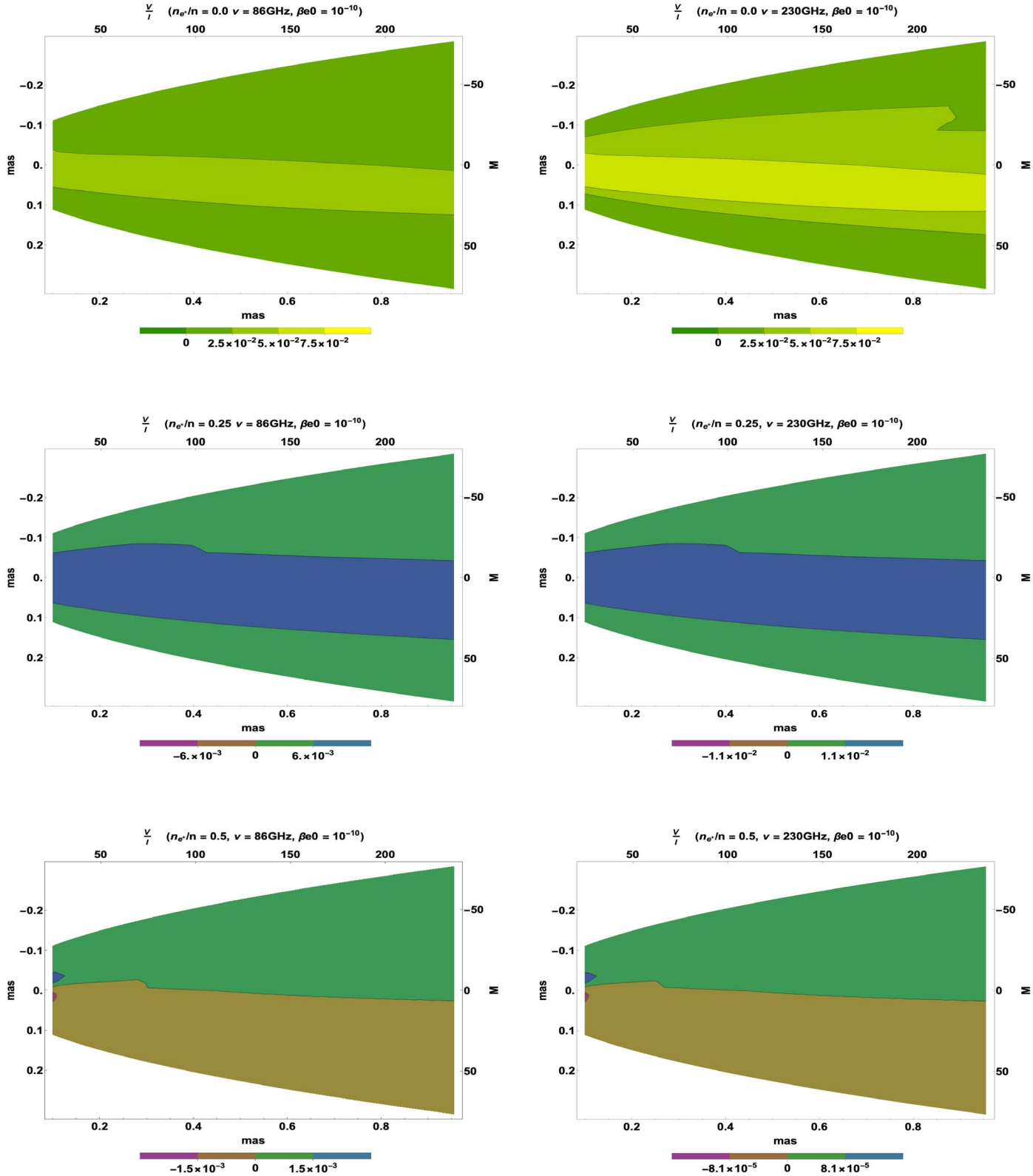

Figure 15. Degree of circular polarization V/I at 86 GHz (left) and 230 GHz (right) for maximally ionic plasma $n_{e^+} = 0$, $n_i = 0.5$ (top), fiducial model plasma $n_{e+} = n/4 = n_i$ and a maximally leptonic plasma $n_{e^+} = n_{e^-} = n/2$, $n_i = 0$ (bottom) for $\beta_{e0} = 10^{-10}$, $\gamma_{\min} = 10$, and $\gamma_{\max} = \infty$.

3. On the other hand, increasing β_{e0} washes out the antisymmetric patterns in the normalized U maps, and does so more rapidly at lower frequencies.
4. Except at high β_{e0}, there is a characteristic frequency, ν^*, above which the autocorrelations of Q and U become degenerate in n_{e^+}/n.

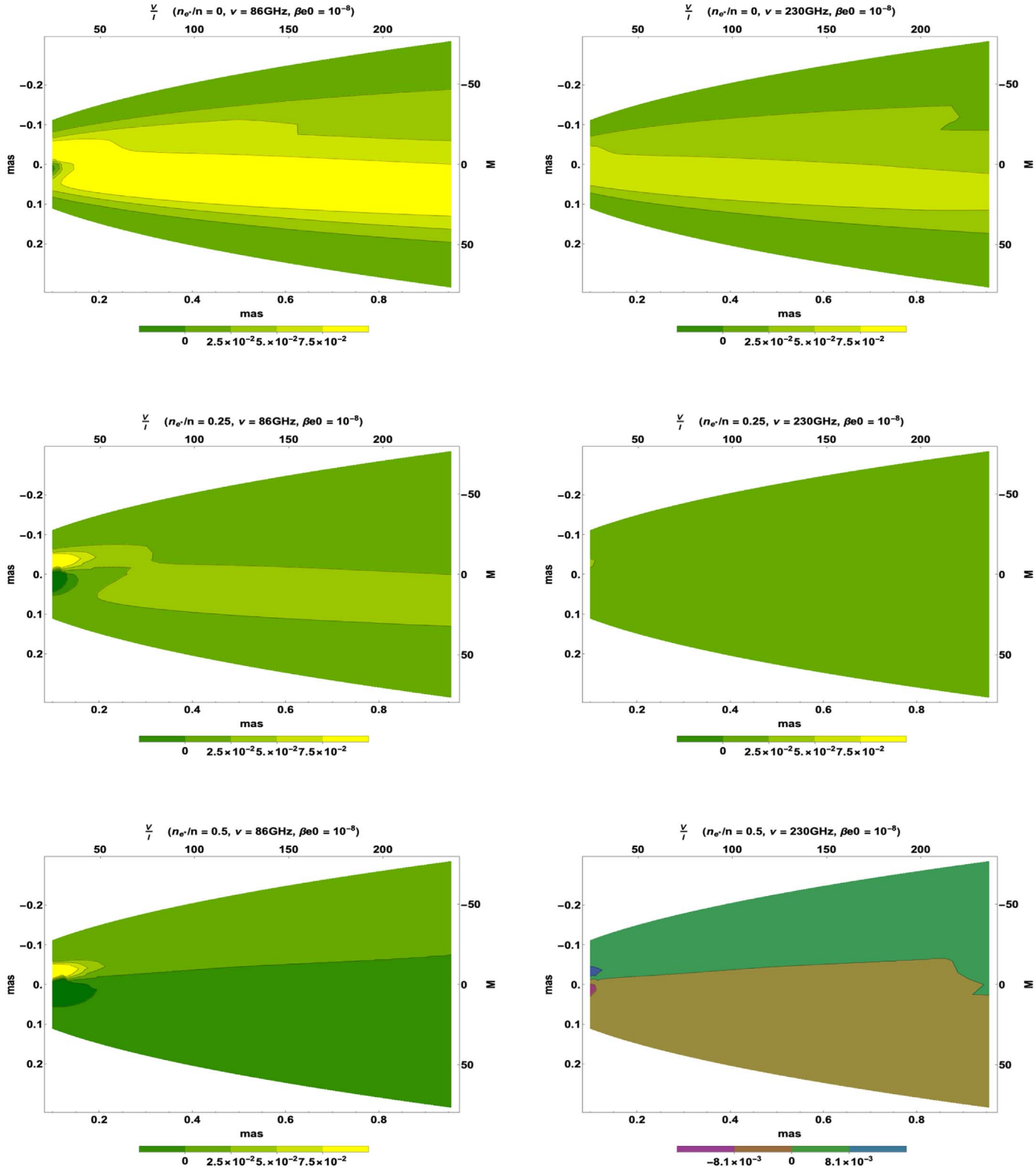

Figure 16. Degree of circular polarization V/I at 86 GHz (left) and 230 GHz (right) for maximally ionic plasma $n_{e^+} = 0$, $n_i = 0.5$ (top), fiducial model plasma $n_{e+} = n/4 = n_i$ and a maximally leptonic plasma $n_{e^+} = n_{e^-} = n/2$, $n_i = 0$ (bottom) for $\beta_{e0} = 10^{-8}$, $\gamma_{\min} = 10$, and $\gamma_{\max} = \infty$.

Owing to these important properties, we claim that multiwavelength observations of the Stokes Q and U parameters can be used to break the degeneracy between β_{e0} and n_{e^+}/n for $\nu \leqslant \nu^*$ and high-β_{e0} parameter limits and shed more light on the composition of the plasma. We note that for a given AGN jet, these findings are sensitive to whether Q and U are defined relative to the observer plane axes in Figure 1, where the forward jet projection expands along the positive Y-axis. Across an ensemble of jets randomly oriented on the observer plane, we expect Q and

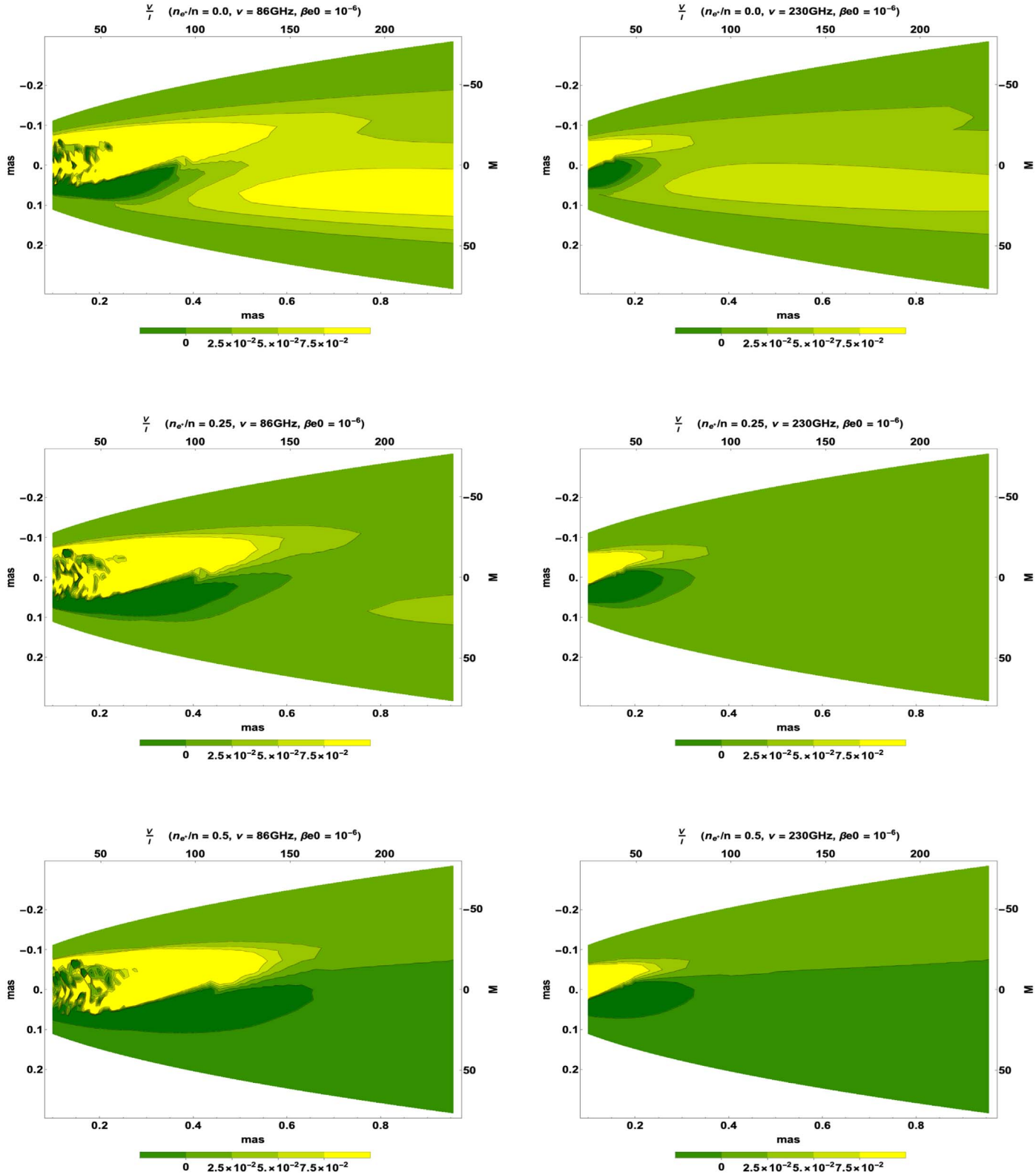

Figure 17. Degree of circular polarization V/I at 86 GHz (left) and 230 GHz (right) for maximally ionic plasma $n_{e^+} = 0$, $n_i = 0.5$ (top), fiducial model plasma $n_{e+} = n/4 = n_i$ and a maximally leptonic plasma $n_{e^+} = n_{e^-} = n/2$, $n_i = 0$ (bottom) for $\beta_{e0} = 10^{-6}$, $\gamma_{\min} = 10$, and $\gamma_{\max} = \infty$.

U to each take on bilaterally symmetric and antisymmetric properties, but for each jet, the $Q - U$ phase difference ensures that the symmetry properties of Q are complementary to those of U at any observer time.

Finally, we calculate the autocorrelation of V, normalize it to $\langle II \rangle$, and take the absolute value. Figure 14 presents $|\langle VV \rangle / \langle II \rangle|$ as a function of the frequency for different values of β_{e0} as well as different plasma compositions.

Table 1
Mean and Maximum Degree of Circular Polarization for Our Models

Model (β_{e0}, n_{e^+}/n, ν)	Mean V/I	Max V/I	Mean $\lvert V/I\rvert$	Max $\lvert V/I\rvert$
(10^{-10}, 0.0, 86 GHz)	3.8×10^{-2}	1.1×10^{-1}	3.8×10^{-2}	1.1×10^{-1}
(10^{-10}, 0.0, 230 GHz)	2.3×10^{-2}	7.1×10^{-2}	2.3×10^{-2}	7.1×10^{-2}
(10^{-10}, 0.25, 86 GHz)	1.3×10^{-2}	3.8×10^{-2}	1.3×10^{-2}	3.8×10^{-2}
(10^{-10}, 0.25, 230 GHz)	7.8×10^{-3}	2.3×10^{-2}	7.8×10^{-3}	2.3×10^{-2}
(10^{-10}, 0.5, 86 GHz)	-2.6×10^{-6}	3.1×10^{-3}	5.3×10^{-5}	3.1×10^{-3}
(10^{-10}, 0.5, 230 GHz)	-1.2×10^{-7}	1.6×10^{-4}	2.8×10^{-6}	1.6×10^{-4}
(10^{-8}, 0.0, 86 GHz)	3.8×10^{-2}	2.1×10^{-1}	3.8×10^{-2}	2.1×10^{-1}
(10^{-8}, 0.0, 230 GHz)	2.3×10^{-2}	6.9×10^{-2}	2.4×10^{-2}	6.9×10^{-2}
(10^{-8}, 0.25, 86 GHz)	1.2×10^{-2}	2.3×10^{-1}	1.4×10^{-2}	2.3×10^{-1}
(10^{-8}, 0.25, 230 GHz)	7.8×10^{-3}	2.8×10^{-2}	7.8×10^{-3}	2.9×10^{-2}
(10^{-8}, 0.5, 86 GHz)	-5.1×10^{-4}	2.5×10^{-1}	5.2×10^{-3}	2.5×10^{-1}
(10^{-8}, 0.5, 230 GHz)	-3.1×10^{-5}	1.6×10^{-2}	2.9×10^{-4}	1.6×10^{-2}
(10^{-6}, 0.0, 86 GHz)	2.7×10^{-2}	5.2×10^{-1}	4.7×10^{-2}	5.2×10^{-1}
(10^{-6}, 0.0, 230 GHz)	2.1×10^{-2}	3.7×10^{-1}	2.7×10^{-2}	3.7×10^{-1}
(10^{-6}, 0.25, 86 GHz)	1.9×10^{-2}	5.5×10^{-1}	3.3×10^{-2}	5.5×10^{-1}
(10^{-6}, 0.25, 230 GHz)	7.9×10^{-3}	3.5×10^{-1}	1.8×10^{-2}	3.5×10^{-1}
(10^{-6}, 0.5, 86 GHz)	9.7×10^{-3}	5.2×10^{-1}	2.7×10^{-2}	3.7×10^{-1}
(10^{-6}, 0.5, 230 GHz)	1.7×10^{-3}	3.4×10^{-1}	1.6×10^{-2}	3.7×10^{-1}

Unlike the normalized autocorrelation functions of Q and U, $|\langle VV\rangle/\langle II\rangle|$ is more sensitive to the plasma composition than to the value of the β_{e0}, with the discriminating effect occuring at high frequency and low β_{e0}. This means that we can further break the aforementioned degeneracy between physical parameters when we combine the analyses of linear and circular polarizations. The observed frequency dependence in $|\langle VV\rangle/\langle II\rangle|$ can be used to predict the plasma composition, while the dependences in $\langle QQ\rangle/\langle II\rangle$ and $\langle UU\rangle/\langle II\rangle$ are used to determine β_{e0}. Taking Figures 13 and 14 together, we can compare with 50–230 GHz Stokes map observations to simultaneously constrain β_{e0} and n_{e+}/n parameters.

6.3. Degree of Polarization

Polarization has been robustly detected in many AGN. M87 has been observed at 86 GHz by the VLBA and Green Bank Telescope to be up to 20% polarized near the core (Hada et al. 2016). The preponderance of this is assumed to be linear polarization from jet regions with highly ordered magnetic fields. Percent-level degrees of circular polarization have been detected in Sgr A* (1.2% ± 0.3% at 230 GHz and 1.6% ± 0.3% at 345 GHz; Munoz et al. 2012) by the Submillimeter Array (SMA) to a precision of tenths of a percent; however, the determination of the source intrinsic circular polarization is more challenging due to the low magnitude of circular polarization and is further confounded by Faraday conversion. The SPRITE proposal at OVRO plans to distinguish among observations of the degree of circular polarization at the 10^{-3} level (R. Blandford 2019, private communication); however, a modeling complication is that the emissivity is sensitive to the pitch angle distribution of the emitting particles (although it is worth calculating assuming an isotropic distribution). We now present maps of the degree of circular polarization for our semianalytical model, with signatures that promise to distinguish observed plasmas with different compositions as an independent approach from our autcorrelation methodology above.

6.3.1. Degree of Circular Polarization

In our models, the degree of circular polarization vanishes for pure e^-e^+ plasma (except for Faraday conversion effects) because the contributions from electrons and positrons almost cancel each other. This is borne out in Figures 15–17, where different legends are used for the lower β_{e0} plots in order to accommodate the suppresion on a few orders of magnitude for the $n_{e^+}/n = 0.5 = n_{e^-}/n$ case. By contrast, plasmas in which at least half of ions carry a positive charge for $\beta_{e0} = 10^{-10}$ (see Figure 15) have V/I at least 5×10^{-3} over most of the observer plane, with mean/maximum values $4.0 \times 10^{-3}/1.2 \times 10^{-2}$ for ($n_{e^+}/n = 0.25$, $\nu = 86$ GHz), $7.8 \times 10^{-3}/2.3 \times 10^{-2}$ for ($n_{e^+}/n = 0.25$, $\nu = 230$ GHz), $1.2 \times 10^{-2}/3.7 \times 10^{-2}$ for ($n_{e^+}/n = 0.0$, $\nu = 86$ GHz) and $2.3 \times 10^{-2}/7.1 \times 10^{-2}$ for ($n_{e^+}/n = 0.0$, $\nu = 230$ GHz) (see Table 1). Mean and maximum degree of circular polarization V/I may differ substantially from the mean and maximum $|V/I|$ over some maps, since more leptonic plasma tends to have more balanced areas of positive versus negative V/I, particularly for lower β_{e0} and higher ν. Over parameter space, the greatest mean V/I, 3.8%, and mean $|V/I|$, 4.7%, are achieved for maximally hadronic plasma, for (β_{e0}, ν) = (10^{-8}, 86 GHz) and (10^{-6}, 86 GHz), respectively. The tenths of a percent and greater circular polarization degrees predicted by several of our models are currently measurable, e.g., by SMA and EHT, or are easily within the realm of possibility for near-future instruments.

7. Conclusions

In this work, we address the long-standing mystery of the plasma composition of relativistic jets not only from the standpoint of intensity, but rather through the lens of all of four Stokes parameters. To this end, we implement a simple subequipartition emission model in which the particle pressure is taken to be fixed fractions of the magnetic pressure in a self-similar, stationary, axisymmetric, M87-based jet model with electrons and varying positive ion versus positron content. Visualizing polarization as Stokes maps as opposed to E-field directions overlaying intensity maps confers the advantage of enabling symmetries to manifest themselves. Among the observational signatures predicted are slight bilateral asymmetry in I and one independent linear polarization, and bilateral antisymmetry in the other. The clearest observable is an enhancement of circular polarization with increasing parameter β_{e0} and ion content n_i/n. Thus, we have the immediate

millimeter to submillimeter observational prospect of inferring e^-e^+ plasmas for $\beta_{e0} \sim 10^{-10}$ if circular polarization is undetectable at the percent level; or mostly p positive charge carriers if $\beta_{e0} \gtrsim 10^{-6}$, and the mean circular polarization across a mas-scale map is at the percent level.

We also considered the autocorrelation functions of the Stokes parameters and normalized them to the intensity function. The normalized autocorrelations of Stokes Q and U increase and decrease with the frequency, respectively. Our computations show that both of these parameters exhibit more sensitivity to the value of β_{e0} than to the plasma composition. The symmetric/antisymmetric patterns of Stokes Q and U correspondingly depend on the value of β_{e0}. Increasing β_{e0} washes out the antisymmetric patterns in the U maps up to a characteristic frequency, ν^*, at which the autocorrelations of linear polarizations become degenerate. The antisymmetric patterns in U become prevalent at higher frequencies. Higher values of β_{e0} enhance the autocorrelation of Stokes I more quickly than that of Stokes Q, thus decreasing the magnitude of $\langle QQ\rangle/\langle II\rangle$ with increasing β_{e0}; higher n_{e^+}/n tends to decrease $\langle QQ\rangle/\langle II\rangle(\omega)$. We may use these as probes indicating that rapid increase in the autocorrelation of a normalized linear polarization may favor lower β_{e0} or higher ionic content. On the other hand, we find that $|VV/II|$ shows more sensitivity to the plasma composition than the value of β_{e0}. Thus, the simultaneous consideration of Q, U, and V can break the degeneracy between the physical parameters n_{e^+}/n and β_{e0} and give us novel information about the underlying physics.

We only used a simple equipartition-inspired emission prescription in our semianalytic model in this work. In the future, we plan to consider other emission models based on velocity shear and jet current density (Anantua et al. 2018). Some models may affect intensity and polarization differently due to different dependencies of the magnetic field strength B on the strengths of the magnetic field components $B_{||}$ and $B_\perp$ with respect to the observer direction. Our model was tuned to the viewing angle of the M87 jet, although sources with smaller viewing angles such as the archetypal blazar 3C 279 are subject to potentially substantial additional Doppler-boosting effects $\propto \mathcal{D}^4$. We could also extend the model using self-similarity to compare a large-scale synthetic jet to observations of jets as cosmic-ray accelerators (Fowler et al. 2019); or change our computational apparatus to a polarized Kerr radiative transfer routine such as GRTRANS (Dexter 2016), postprocessing a time-dependent simulations such as KORAL (Sadowski et al. 2016; Chael et al. 2019) to compare our models with AGN observations near the black hole.

R.A. and R.E. acknowledge support by the Institute for Theory and Computation at the Center for Astrophysics | Harvard and Smithsonian. This work was supported in part by the Black Hole Initiative at Harvard University, which is funded by grants from the John Templeton Foundation and the Gordon and Betty Moore Foundation.

Facilities: VLA:43 GHz, EHT:230 GHz.

Software: Mathematica (version 11.3.0, Wolfram 2018).

Appendix A
Generalized Emission and Absorption Coefficients

We find radiative transfer coefficients for a power-law distribution of electrons and positrons,

$$N'_{e\Omega'}(\gamma') = K'_{e\Omega'}\gamma'^{-p} \tag{A1}$$

$$n'_{e\Omega'} = \int_1^\infty N'_{e\Omega'}(\gamma')d\gamma' = K'_{e\Omega'}\frac{-1}{1-p}\gamma^{1-p}\Big]_{\gamma=1}^{\infty} = K'_{e\Omega'}\frac{1}{p-1} \tag{A2}$$

from Anantua (2016), then generalize to $\gamma_{\min} > 1$ a cutoff power law based upon mks formulae from Dexter (2016; note that their formulae are in cgs).

The angular distribution satisfies

$$n'_e = \int_{\Omega'} n'_{e\Omega'}(\boldsymbol{k})d\Omega' \tag{A3}$$

,and for isotropic emitters,

$$n'_{e\Omega'}(\boldsymbol{k}) = \frac{n'_e}{4\pi} \Rightarrow K'_{e\Omega'} = \frac{p-1}{4\pi}n'_e. \tag{A4}$$

The partial pressure due to electrons and positrons emitting near the observed frequency is

$$\tilde{P}_e = \frac{4\pi}{3}\gamma'^2 N'_{e\Omega'}(\gamma')m_e c^2 = \frac{4\pi}{3}K'_{e\Omega'}m_e c^2\gamma'^{2-p}, \tag{A5}$$

where, linking a Lorentz factor to twice the critical frequency, we have

$$\nu' = 2\nu_c\gamma'^2 = \frac{3eB'_\perp}{2\pi m_e c}\gamma'^2 \Rightarrow \tag{A6}$$

$$\tilde{P}_e = \frac{4\pi}{3}K'_{e\Omega'}m_e c^2\left(\frac{3eB'_\perp}{2\pi\nu' m_e}\right)^{\frac{p-2}{2}} \tag{A7}$$

Note that the critical frequency is related to the gyrofrequency ν_B of an electron around a magnetic field line through $\nu_c = \frac{3}{2}\nu_B$. The comoving emissivity coefficient $j_{\nu\Omega}$ from Anantua (2016), where $r_e = k_e\frac{e^2}{m_e c^2}$ is the classical electron radius, is

$$\begin{aligned} j'_{\nu\Omega'} &= \frac{3^{1/2}}{2}\frac{\nu'}{c}r_e\tilde{P}_e\left(\frac{3eB_\perp}{2\pi\nu' m_e}\right)^{\frac{3}{2}}\frac{\Gamma\left(\frac{3p-1}{12}\right)\Gamma\left(\frac{3p+19}{12}\right)}{p+1} \\ &= \frac{3^{1/2}}{2}\frac{\nu'}{c}\frac{k_e e^2}{m_e c^2}\frac{4\pi}{3}K'_{e\Omega'}m_e c^2\left(\frac{3eB_\perp}{2\pi\nu' m_e}\right)^{\frac{p-2}{2}} \\ &\quad\times\left(\frac{3eB_\perp}{2\pi\nu' m_e}\right)^{\frac{3}{2}}\frac{\Gamma\left(\frac{3p-1}{12}\right)\Gamma\left(\frac{3p+19}{12}\right)}{p+1} \\ &= K_{e\Omega'}k_e\frac{2\pi}{3^{1/2}}\frac{\nu' e^2}{c}\left(\frac{3e}{2\pi\nu' m_e}\right)^{\frac{p+1}{2}} \\ &\quad\times B_\perp^{\frac{p+1}{2}}\nu'^{-\frac{p+1}{2}}\frac{1}{p+1}\Gamma\left(\frac{3p-1}{12}\right)\Gamma\left(\frac{3p+19}{12}\right) \\ &= K_{e\Omega'}k_e 2\pi 3^{p/2}\frac{e^2}{c}\left(\frac{e}{2\pi\nu' m_e}\right)^{\frac{p+1}{2}} \\ &\quad\times B_\perp^{\frac{p+1}{2}}\nu'^{\frac{1-p}{2}}\frac{1}{p+1}\Gamma\left(\frac{3p-1}{12}\right)\Gamma\left(\frac{3p+19}{12}\right). \end{aligned} \tag{A8}$$

The corresponding equation in Dexter (2016; which uses cgs) is

$$j'_{0I} = \frac{e^2}{c}\left(\frac{e}{2\pi m_e c}\right)^{\frac{p+1}{2}} (n'_{e^-} + n'_{e^+})\, B'^{(p+1)/2}_{\perp} \nu'^{\frac{1-p}{2}} \times \left(\frac{3^{\frac{p}{2}}(p-1)}{2(p+1)}\right) \times \frac{\Gamma\left(\frac{3p-1}{12}\right)\Gamma\left(\frac{3p+19}{12}\right)}{(\gamma'^{1-p}_{\min} - \gamma'^{1-p}_{\max})}. \tag{A9}$$

Using cgs to SI conversions for factors corresponding to the Coulomb coupling and gyrofrequency (see Appendix B of Cawthorne & Hughes 2014),

$$\begin{cases} \dfrac{e^2}{c} \to \dfrac{e^2}{4\pi\epsilon_0 c} \\ \dfrac{eB}{\pi m_e c} \to \dfrac{eB}{\pi m_e} \end{cases}, \tag{A10}$$

we have

$$\frac{(j'_{\nu\Omega'})_{\rm cgs}}{j'_{0I}} = \frac{4\pi K'_{e\Omega'}}{(n_{e-} + n_{e+})(p-1)\frac{1}{\gamma^{1-p}_{\min} - \gamma^{1-p}_{\max}}} = \gamma^{1-p}_{\min} - \gamma^{1-p}_{\max}. \tag{A11}$$

A natural generalization of the Anantua (2016) analysis to the cutoff power-law distributions of Dexter (2016) is to divide these coefficients by the factor $\gamma^{1-p}_{\min} - \gamma^{1-p}_{\max}$, which goes to unity as $\gamma_{\min} \to 1$ and $\gamma_{\max} \to \infty$, as expected.

The linearly polarized emissivites are related by

$$\sqrt{(j'_{Q\nu\Omega'}\cos 2\psi)^2 + (j'_{U\nu\Omega'}\sin 2\psi)^2} = \frac{3(p+1)}{3p+7} j'_{\nu\Omega'}. \tag{A12}$$

The remaining emissivities are computed on the $U = 0$ basis as

$$\frac{j'_{V\nu'\Omega'}}{j'_{\nu'\Omega'}} = \mathcal{D}^{\frac{1}{2}} \frac{n_{e-} - n_{e+}}{n_{e-} + n_{e+}} \left(\frac{eB_\perp}{2\pi m_e}\right)^{\frac{1}{2}} 3^{-\frac{1}{2}} \frac{B_\parallel}{\nu^{\frac{1}{2}} B_\perp} \times \frac{(p+2)(p+1)}{p} \times \frac{\Gamma\left(\frac{3p+4}{12}\right)\Gamma\left(\frac{3p+8}{12}\right)}{\Gamma\left(\frac{3p-1}{12}\right)\Gamma\left(\frac{3p+19}{12}\right)}. \tag{A13}$$

The absorption coefficient

$$\begin{aligned} \chi'_{\nu'\Omega'} &= \frac{3^{1/2}}{4}\frac{r_e}{m_e \nu' c}\tilde{P}_e \left(\frac{3eB_\perp}{2\pi\nu' m_e}\right)^2 \Gamma\left(\frac{3p+2}{12}\right)\Gamma\left(\frac{3p+22}{12}\right) \\ &= \frac{3^{1/2}}{4}\frac{k_e e^2}{m_e c^2}\frac{1}{m_e \nu' c}\frac{4\pi}{3} K'_{e\Omega'} m_e c^2 \\ &\quad \times \left(\frac{3e}{2\pi\nu' m_e}\right)^{\frac{p}{2}+1} B_\perp^{\frac{p}{2}+1} \frac{3p+10}{12}\Gamma\left(\frac{3p+10}{12}\right)\Gamma\left(\frac{3p+2}{12}\right) \\ &= K'_{e\Omega'}\frac{\pi}{4 \times 3^{1/2}}(3p+10)\frac{k_e e^2}{m_e c^2 \nu'} \\ &\quad \times \left(\frac{3e}{2\pi\nu' m_e}\right)^{\frac{p}{2}+1} B_\perp^{\frac{p}{2}+1}\Gamma\left(\frac{3p+10}{12}\right)\Gamma\left(\frac{3p+2}{12}\right) \\ &= k_e K'_{e\Omega'}\frac{\pi}{4} 3^{\frac{p-1}{2}}(3p+10)\frac{e^2}{m_e c^2}\nu'^{-\frac{p}{2}-2} \\ &\quad \times \left(\frac{e}{2\pi m_e}\right)^{\frac{p}{2}+1} B_\perp^{\frac{p}{2}+1}\Gamma\left(\frac{3p+10}{12}\right)\Gamma\left(\frac{3p+2}{12}\right). \end{aligned} \tag{A14}$$

The corresponding absorption coefficient in Dexter (2016) is

$$\chi'_{0I} = \frac{e^2}{16 m_e c}\left(\frac{e}{2\pi m_e c}\right)^{\frac{p+2}{2}} 3^{\frac{p-1}{2}}(n'_{e^-} + n'_{e^+}) B'^{(p+2)/2}_\perp \nu'^{-\frac{p}{2}-2} \times (p-1)(3p+10)\frac{\Gamma\left(\frac{3p+10}{12}\right)\Gamma\left(\frac{3p+2}{12}\right)}{(\gamma'^{1-p}_{\min} - \gamma'^{1-p}_{\max})}. \tag{A15}$$

Then

$$\frac{(\chi'_{\nu\Omega'})_{\rm cgs}}{\chi'_{0I}} = \frac{\frac{\pi}{4}K'_{e\Omega'}}{(n_{e-} + n_{e+})\frac{1}{16}(p-1)\frac{1}{\gamma^{1-p}_{\min} - \gamma^{1-p}_{\max}}} = \gamma^{1-p}_{\min} - \gamma^{1-p}_{\max}. \tag{A16}$$

The linearly polarized absorption coefficients are related by

$$\sqrt{(\chi'_{Q\nu\Omega'}\cos 2\psi)^2 + (\chi'_{U\nu\Omega'}\sin 2\psi)^2} = \frac{3(p+2)}{3p+10}\chi'_{\nu\Omega'}. \tag{A17}$$

Appendix B
Faraday Rotation and Absorption Coefficients

The Faraday coefficients were not included in the Anantua (2016) work, but are adopted from Dexter (2016),

$$(\rho'_{0Q})_{\rm cgs} = -(n'_{e^-} + n'_{e^+})\frac{p-1}{\gamma'^{1-p}_{\min} - \gamma'^{1-p}_{\max}}\gamma'^{2-p}_{\min} \times \frac{1 - \left(\frac{eB'_\perp}{2\pi m_e c}\gamma'^2_{\min}\nu'^{-1}\right)^{\frac{p}{2}-1}}{\frac{p}{2}-1} c\left(\frac{e^2}{m_e c^2}\right)\left(\frac{eB'_\perp}{2\pi m_e c}\right)^2 \nu'^{-3}, \tag{B1}$$

$$(\rho'_{0V})_{\rm cgs} = (n'_{e^-} - n'_{e^+})\frac{p-1}{\gamma'^{1-p}_{\min} - \gamma'^{1-p}_{\max}}\frac{p+2}{p+1}\gamma'^{-(p+1)}_{\min}\ln\gamma_{\min} \times c\left(\frac{e^2}{m_e c^2}\right) 2\left(\frac{eB'_\perp}{2\pi m_e c}\right)\frac{B'_\parallel}{B'_\perp}\nu'^{-2} \tag{B2}$$

now converted from cgs into SI through

$$\begin{cases} (\nu_B)_{\rm SI} = c(\nu_B)_{\rm cgs} \\ (\rho_\perp)_{\rm SI} = \dfrac{1}{4\pi\epsilon_0}\dfrac{1}{c}(\rho_\perp)_{\rm cgs} \end{cases} \Rightarrow \begin{cases} (\rho_V)_{\rm SI} = \dfrac{1}{4\pi\epsilon_0}c(\rho_V)_{\rm cgs} \\ (\rho_{\rm FC})_{\rm SI} = \dfrac{1}{4\pi\epsilon_0}c^2(\rho_{\rm FC})_{\rm cgs} \end{cases} \tag{B3}$$

into

$$(\rho'_{0Q})_{\rm SI} = -(n'_{e^-} + n'_{e^+})\frac{p-1}{\gamma'^{1-p}_{\min} - \gamma'^{1-p}_{\max}}\gamma'^{2-p}_{\min} \times \frac{1 - \left(\frac{eB'_\perp}{2\pi m_e c}\gamma'^2_{\min}\nu'^{-1}\right)^{\frac{p}{2}-1}}{\frac{p}{2}-1} c\left(\frac{e^2}{4\pi\epsilon_0 m_e c^2}\right)\left(\frac{eB'_\perp}{2\pi m_e}\right)^2 \nu'^{-3}, \tag{B4}$$

$$= -(n'_{e^-} + n'_{e^+}) \frac{p-1}{\gamma'^{1-p}_{\min} - \gamma'^{1-p}_{\max}} \gamma'^{2-p}_{\min} \times \left(\frac{1 - \frac{3^{\frac{4-p}{2}}}{4\pi} \gamma'^{p-2}_{\min} \frac{1}{K'_{\Omega'} m_e c^2} \tilde{P}_e}{\frac{p}{2} - 1} \right) c \left(\frac{e^2}{4\pi\epsilon_0 m_e c^2} \right) \left(\frac{eB'_\perp}{2\pi m_e} \right)^2 \nu'^{-3}, \tag{B5}$$

$$(\rho'_{0V})_{\rm SI} = (n'_{e^-} - n'_{e^+}) \frac{p-1}{\gamma'^{1-p}_{\min} - \gamma'^{1-p}_{\max}} \frac{p+2}{p+1} \gamma'^{-(p+1)}_{\min} \ln \gamma_{\min} \times c \left(\frac{e^2}{4\pi\epsilon_0 m_e c^2} \right) \left(\frac{e}{\pi m_e c} \right) B'_{||} \nu'^{-2}, \tag{B6}$$

where we have used Equation (A7) to substitute $\frac{eB'_\perp}{2\pi m_e} = \left[\left(\frac{3}{\nu'} \right)^{\frac{2-p}{2}} \frac{\tilde{P}_e}{\frac{4\pi}{3} K'_{\Omega'} m_e c^2} \right]^{\frac{2}{p-2}} = \frac{\nu'}{3} \left(\frac{3\tilde{P}_e}{4\pi K'_{\Omega'} m_e c^2} \right)^{\frac{2}{p-2}}$,

ORCID iDs

Richard Anantua https://orcid.org/0000-0003-3457-7660
Abraham Loeb https://orcid.org/0000-0003-4330-287X
Andrew Chael https://orcid.org/0000-0003-2966-6220

References

Ackermann, M., Anantua, R., Asano, K., et al. 2016, ApJL, 824, L20
Anantua, R. 2016, PhD thesis, Stanford Univ.
Anantua, R., Blandford, R., & Tchekhovskoy, A. 2018, Galax, 6, 31
Anantua, R., Ressler, S., & Quataert, E. 2020, MNRAS, 493, 1404
Begelman, M., Blandford, R., & Rees, M. 1984, RvMP, 56, 255
Blandford, R., & Anantua, R. 2017, JPhCS, 840, 012023
Blandford, R. D., & Payne, D. G. 1982, MNRAS, 199, 883
Blandford, R. D., & Znajek, R. L. 1977, MNRAS, 179, 433
Bourouaine, S., Verscharen, D., Chandran, B. D. G., Marauca, B. A., & Kasper, J. C. 2018, ApJL, 777, L3
Cawthorne, T. V., & Hughes, P. A. 2014, ApJ, 771, 60
Chael, A., Narayan, R., & Johnson, M. D. 2019, MNRAS, 486, 2873
Curtis, H. D. 1918, PLicO, 13, 9
Dexter, J. 2016, MNRAS, 462, 115
Enßlin, T. A., Hutschenreuter, S., & Gopal-Krishna 2019, JCAP, 2019, 035
Event Horizon Telescope Collaboration 2019, ApJL, 875, L1
Fowler, K., Li, H., & Anantua, R. 2019, ApJ, 885, 4
Gebhardt, K., Adams, J., Richastone, D., et al. 2011, ApJ, 729, 119
Hada, K., Kino, M., Akihiro, D., et al. 2016, ApJ, 817, 2
Hawley, J. F., & Krolik, J. H. 2006, ApJ, 641, 103
Jones, T. W., & Odell, S. L. 1977, ApJ, 214, 522
Kim, J. Y., Krichbaum, T. P., Broderick, A., et al. 2020, A&A, in press
Kim, J. Y., Krichbaum, T. P., Lu, R. S., et al. 2018, A&A, 616, A188
Marrone, D. P., Moran, J. M., Zhao, J. H., & Rao, R. 2007, ApJ, 654L, 57
McKinney, J. C., & Blandford, R. 2009, MNRAS, 394, L126
McKinney, J. C., Gammie, C. F., & Toth, G. 2003, ApJ, 589, 444
McKinney, J. C., Tchekhovskoy, A., & Blandford, R. 2012, MNRAS, 423, 3083
Melrose, D. B. 1971, Ap&SS, 12, 172
Mościbrodzka, M., Falcke, H., & Noble, S. 2016, A&A, 596, A13
Munoz, D. J., Marrone, D. P., Moran, J. M., & Rao, R. 2012, ApJ, 745, 115
Park, K., & Blackman, E. G. 2010, MNRAS, 403, 1993
Pierre Auger Collaboration 2017, Sci, 357, 1266
Prieto, M. A., Fernandez-Ontiveros, J. A., Markoff, S., Espada, D., & Gonzalez-Martin, O. 2016, MNRAS, 457, 3801
Rees, M. J. 1968, ApJL, 2, L1
Ressler, S. M., Tchekhovskoy, A., Quataert, E., Chandra, M., & Gammie, C. F. 2015, MNRAS, 454, 1848
Ressler, S. M., Tchekhovskoy, A., Quataert, E., & Gammie, C. F. 2017, MNRAS, 467, 3604
Ruszkowski, M., & Begelman, M. C. 2002, ApJ, 573, 485
Rybicki, G., & Lightman, A. 2004, Radiative Processes in Astrophysics (2nd ed.; Weinheim: Verlag GmbH & Co. KGaA)
Sadowski, A., Wielgus, M., Narayan, R., et al. 2016, MNRAS, 466, 705
Walker, R. C., Hardee, P. E., Davies, F. B., Ly, C., & Junor, W. 2018, ApJ, 855, 128
Wardle, J. F. C., Homan, D. C., Ojha, R., & Roberts, D. H. 1998, Natur, 395, 457
Westfold, K. C. 1959, ApJ, 130, 241
Wolfram 2018, Mathematica, v.11.3.0, (Champaign, IL: Wolfram Research)